Journal of Structural Geology 33 (2011) 1378–1393

Contents lists available at ScienceDirect

Journal of Structural Geology

journal homepage: www.elsevier.com/locate/jsg

Deformation of an elliptical inclusion in two-dimensional incompressible power-law viscous flow

Neil S. Mancktelow

Department of Earth Sciences, Geologisches Institut, ETH Zurich, Zurich, Switzerland

ARTICLE INFO

Article history:
Received 3 January 2011
Received in revised form
3 June 2011
Accepted 17 June 2011
Available online 29 June 2011

Keywords:
Inclusion
Particle
Power-law viscous flow
Shear zone
Strain measurement

ABSTRACT

An iterative, semi-analytical solution is derived for deformation of an elliptical (in cross-section) power-law viscous inclusion within an infinite linear viscous matrix undergoing a general 2D incompressible flow. Finite-element numerical models are used to extend the analysis to that of a power-law viscous matrix. The general behaviour of a deformable elliptical inclusion is not dramatically changed by power-law viscous rheology, but the effective viscosity is now a function of the orientation and axial ratio of the inclusion. Overall, the effect is similar to a markedly increased viscosity ratio for a stronger inclusion, or a decreased ratio for a weaker inclusion, when compared to the linear viscous case. As a result, rather low reference state viscosity ratios between inclusion and matrix (e.g., 2 to 3, determined at the same effective strain rate for both materials) can produce marked differences in behaviour for the range of power-law stress exponents established experimentally for many minerals and rocks (typically 3–6). Even for very high strain within a shear zone ($\gamma > 100$), initially nearly circular inclusions ($R < 2$) can maintain low axial ratios ($R < 2$–3) and widely variable orientations. These inclusions deform internally and are not rigid, but continue to rotate or oscillate without strong elongation.

1. Introduction

Rocks are never homogeneous and clasts, particles and grains are ubiquitous over a wide scale range, from microns to kilometres. These inclusions are generally irregular in shape and may be closely packed. However, in some important natural examples, such as isolated porphyroclasts, pebbles in matrix-supported conglomerates, and widely dispersed oolites in some limestones, particles may be sufficiently separated that they do not interact during deformation and can be well approximated as an isolated rigid or viscous inclusion embedded in an infinite isotropic viscous matrix (e.g., Ildefonse et al., 1992b; Treagus and Treagus, 2002; Mandal et al., 2003). Several previous studies considering 2D flow have shown that, at least for effectively rigid particles, the enclosing ellipse provides a good approximation to the rotational behaviour of more complex inclusion shapes (Bretherton, 1962; Willis, 1977; Ferguson, 1979; Fernandez et al., 1983; Arbaret et al., 2001; Schmid, 2005) and the results for elliptical inclusions are therefore more generally applicable. For deformable particles, the actual inclusion shape may have a more significant effect (Treagus and Lan, 2003) and shape is also important for particles that are weakly bonded to the matrix, where parallelepiped forms promote the development of stable orientations during shearing (Pennacchioni et al., 2001; Mancktelow et al., 2002).

Analytical solutions have been derived for the behaviour of (1) rigid particles in an isotropic linear viscous matrix (Jeffery, 1922; Bretherton, 1962; Ghosh and Ramberg, 1976); (2) isotropic linear viscous deformable inclusions in an isotropic linear viscous matrix (Bilby et al., 1975; Howard and Brierley, 1976; Bilby and Kolbuszewski, 1977; Schmid and Podladchikov, 2003; Mulchrone and Walsh, 2006), and (3) rigid inclusions (Mandal et al., 2005a) or, more generally, linear viscous, rigid and inviscid inclusions (Fletcher, 2009) in an anisotropic linear viscous matrix. However, the crystal-plastic flow of most rocks and minerals is more realistically described by a power-law rheology (e.g., Kohlstedt et al., 1995).

Many numerical and analogue modelling studies have considered power-law behaviour of the inclusion and/or matrix when investigating, for example, the rotation and interaction of rigid particles (Ferguson, 1979; Ildefonse and Mancktelow, 1993), the deformation of strong, but not rigid, isolated clasts (e.g., calcite clasts in quartz mylonites; Mancktelow and Pennacchioni, 2010a), the development of mantled porphyroclasts (Passchier and Sokoutis, 1993) and their use as indicators of the stress sensitivity in power-law viscous materials (Passchier et al., 1993), the folding of a power-law layer of finite length, modelled as an elliptical inclusion

E-mail address: neil@erdw.ethz.ch.

0191-8141/$ – see front matter © 2011 Elsevier Ltd. All rights reserved.
doi:10.1016/j.jsg.2011.06.005

(Schmid et al., 2004), the nucleation and propagation of shear zones initiated on isolated weaker circular inclusions (Grujic and Mancktelow, 1998; Mancktelow, 2002, 2006), and the more general behaviour of two-phase power-law viscous mixtures (Jessell et al., 2009). To my knowledge, the only analytical investigation specifically considering the behaviour of a power-law viscous inclusion is that of Gilormini and Montheillet (1986), which was further developed and compared to numerical finite-element models in Gilormini and Germain (1987). Schmid et al. (2004) also considered a power-law viscous elliptical inclusion embedded in a linear viscous matrix as a model for folding of an isolated layer of finite length. However, in these three publications, only the simplified case of pure shear with inclusion axes parallel to the principal axes was considered, which does not provide information on the rotational behaviour of the inclusion.

In this study, the linear viscous analytical solution of Bilby and Kolbuszewski (1977) is extended to the case of a power-law viscous inclusion for all inclusion orientations and for 2D incompressible slow flows covering the range from pure to simple shear. Numerical finite-element models are used to additionally investigate the effects of power-law viscous rheology for both inclusion and matrix. General characteristics of inclusion behaviour that are independent of rheology are summarized and the results for power-law viscous rheology of the inclusion and/or matrix compared and contrasted to linear viscous behaviour. MATLAB scripts for calculating the results presented here are provided in the Supplementary material.

2. Previous work

2.1. Overview

A mathematical treatment of an isolated rigid spherical inclusion in a linear viscous matrix was first developed by Einstein (1906, 1911). This was extended by Jeffery (1922) to particles of ellipsoidal shape, with a complete solution presented for an ellipsoid of revolution (i.e., an axisymmetric shape), as also considered by Bretherton (1962). The more general case of a triaxial ellipsoid requires numerical integration (e.g., Gierszewski and Chaffey, 1978; Hinch and Leal, 1979; Freeman, 1985; Jiang, 2007a). Ghosh and Ramberg (1976) combined the results of Jeffery (1922) and Muskhelishvili (1953) to provide analytical solutions for the rotational behaviour of a rigid elliptical particle in a general 2D incompressible flow ranging from pure to simple shear. They then compared these results to analogue model experiments in simple shear. Details of the rotational behaviour of rigid particles and possible factors that could hinder this rotation have been the subject of many other studies, reflecting the importance of the subject for understanding deformed natural rocks (e.g., Gay, 1968; Ghosh and Sengupta, 1973; Ferguson, 1979; Fernandez et al., 1983; Freeman, 1985; Passchier and Simpson, 1986; Passchier, 1987; Ildefonse and Fernandez, 1988; Ildefonse et al., 1992a, b; Ildefonse and Mancktelow, 1993; Passchier and Sokoutis, 1993; Ježek, 1994; Ježek et al., 1994, 1996; Bjørnerud and Zhang, 1995; Marques and Cobbold, 1995; ten Brink and Passchier, 1995; Arbaret et al., 1996, 2001; Pennacchioni et al., 2000; Marques and Coelho, 2001; Mancktelow et al., 2002; Piazolo et al., 2002; Piazolo and Passchier, 2002; ten Grotenhuis et al., 2002; Ceriani et al., 2003; Mandal et al., 2003, 2005b, c; Fletcher, 2004; Marques and Bose, 2004; Marques, 2005; Marques et al., 2005a, b, c; Jiang, 2007a; Fay et al., 2008; Jessell et al., 2009; Johnson et al., 2009).

Solutions for an isolated deformable ellipsoidal inclusion in an infinite matrix were initially established for linear elasticity (Robinson, 1951; Muskhelishvili, 1953; Eshelby, 1957, 1959). In deriving his solution, Eshelby (1957) proposed that the stress (and strain) within an isolated ellipsoidal inclusion in an infinite linear elastic matrix is homogeneous. This has become known as the "Eshelby conjecture" and been demonstrated to hold true regardless of the rheology of the inclusion if the matrix is linear elastic or linear viscous (e.g. Bilby and Kolbuszewski, 1977; Schmid and Podladchikov, 2003). Several studies have subsequently transformed the original elastic solutions to the directly corresponding case of an isotropic linear viscous deformable inclusion in an isotropic linear viscous matrix (e.g., Bilby et al., 1975; Howard and Brierley, 1976; Bilby and Kolbuszewski, 1977; Schmid and Podladchikov, 2003; Mulchrone and Walsh, 2006), and Jiang (2007b, in press) developed interactive routines to allow easy calculation and visualization of the 3D results.

2.2. Results for linear viscous rheology and 2D flow

A summary of the full 3D solution for linear viscous rheology, based largely on the work of Eshelby (1957, 1959) and Bilby et al. (1975), is provided in Jiang (2007b). Here only the simpler 2D case is considered, mainly following Bilby and Kolbuszewski (1977). The basic 2D geometry of an isolated inclusion with an elliptical cross-section is presented in Fig. 1, with the $x_{1'}$-$x_{2'}$ axes defined as the external reference frame and the x_1-x_2 axes fixed to the semi-axes of the elliptical inclusion. The angle ψ is measured (counter-clockwise positive) between the external $x_{1'}$ axis and the long axis of the inclusion parallel to x_1. R is used here to denote the axial ratio of the inclusion (Fig. 1) (e.g., Ramsay, 1967; Dunnet, 1969; Ghosh and Ramberg, 1976; Lisle, 1985; Pennacchioni et al., 2001; Mandal et al., 2005a), whereas Bilby and Kolbuszewski (1977) used σ for the axial ratio and R for the viscosity ratio of inclusion to matrix (here referred to as δ).

Consider the velocity gradient tensor **L** for the flow in the matrix at infinity, with components

$$L_{i'j'} = \frac{\partial v_{i'}}{\partial x_{j'}} \tag{1}$$

in terms of a mixture of pure shear with rate $\dot{e}$ and simple shear with rate $\dot{\gamma}$ so that

$$\mathbf{L} = \begin{bmatrix} \dot{e} & \dot{\gamma} \\ 0 & -\dot{e} \end{bmatrix} = \mathbf{D} + \mathbf{W} \tag{2}$$

where **D** is the symmetric *rate of deformation* tensor

$$\mathbf{D} = \begin{bmatrix} \dot{\epsilon}_{1'1'} & \dot{\epsilon}_{1'2'} \\ \dot{\epsilon}_{1'2'} & \dot{\epsilon}_{2'2'} \end{bmatrix} = \begin{bmatrix} \dot{e} & \frac{\dot{\gamma}}{2} \\ \frac{\dot{\gamma}}{2} & -\dot{e} \end{bmatrix} = \begin{bmatrix} q & s \\ s & -q \end{bmatrix} \tag{3}$$

with components equivalent to

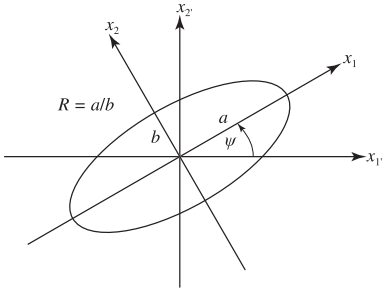

Fig. 1. 2D geometry of an elliptical inclusion, which is cylindrical in the third dimension, with the cylinder axis parallel to the vorticity vector of the 2D flow in the matrix. Axes $x_{1'}$-$x_{2'}$ are the external fixed reference frame used to describe the flow in the matrix, axes x_1-x_2 are parallel to the semi-axes of the inclusion a and b, with axial ratio of the inclusion $R = a/b$.

$$\dot{\epsilon}_{i'j'} = \frac{1}{2}\left(\frac{\partial v_{i'}}{\partial x_{j'}} + \frac{\partial v_{j'}}{\partial x_{i'}}\right) \tag{4}$$

and **W** is the anti-symmetric *vorticity* tensor

$$\mathbf{w} = \begin{bmatrix} 0 & \omega_{1'2'} \\ -\omega_{1'2'} & 0 \end{bmatrix} = \begin{bmatrix} 0 & \frac{\dot{\gamma}}{2} \\ -\frac{\dot{\gamma}}{2} & 0 \end{bmatrix} = \begin{bmatrix} 0 & p \\ -p & 0 \end{bmatrix} = \begin{bmatrix} 0 & s \\ -s & 0 \end{bmatrix} \tag{5}$$

with components equivalent to

$$\omega_{i'j'} = \frac{1}{2}\left(\frac{\partial v_{i'}}{\partial x_{j'}} - \frac{\partial v_{j'}}{\partial x_{i'}}\right). \tag{6}$$

In Eq.'s (3) and (5) above, the shorthand terms q, s and p correspond to the terminology of Bilby and Kolbuszewski (1977), with $\dot{\epsilon}_{1'1'} = -\dot{\epsilon}_{2'2'} = q = \dot{e}$ and $\omega_{1'2'} = s = p = \frac{\dot{\gamma}}{2}$. Implicit in the definitions of Eq.'s (3) and (4) is that $\dot{\gamma}$ is positive for dextral shear and q is positive for extension parallel to $x_{1'}$ (transpression in the case of mixed shear).

The eigenvectors of **D**, with coordinates relative to the $x_{1'}$-$x_{2'}$ axis system of $\left(1, -\frac{1}{s}(\sqrt{q^2+s^2}+q)\right)$ and $\left(1, \frac{1}{s}\left(\sqrt{q^2+s^2}-q\right)\right)$, represent the principal directions of the rate of stretch, commonly called the "instantaneous stretching axes" ISA (e.g., Passchier and Trouw, 2005). The corresponding eigenvalues, $-\sqrt{q^2+s^2}$ and $\sqrt{q^2+s^2}$, are the stretching rates in these principal directions. Using the trigonometric identity that $\tan 2\theta = \frac{2\tan\theta}{1-\tan^2\theta}$, it is readily established that the angle θ between the ISA and $x_{1'}$ is given by

$$\tan 2\theta = \frac{s}{q} = \frac{\dot{\gamma}}{2\dot{e}} = \frac{1}{2s_r}, \tag{7}$$

where, following the definition of Ghosh and Ramberg (1976),

$$s_r = \frac{\dot{e}}{\dot{\gamma}} = \frac{q}{2s}. \tag{8}$$

The eigenvectors of **L** represent the "flow apophyses" (Ramberg, 1975a, b), with flow converging toward the extending eigenvector (parallel to the $x_{1'}$ axis for transpression), and diverging away from the shortening eigenvector (parallel to the $x_{1'}$ axis for transtension). The angle α between the two eigenvectors is given by

$$\alpha = -\tan^{-1}(2s_r) \tag{9}$$

(Bobyarchick, 1986). The angle α decreases from 90° for pure shear ($s_r = \infty$) to 0° for simple shear ($s_r = 0$), in which case the single (non-stretching) eigenvector is parallel to the shear direction $x_{1'}$ (Bobyarchick, 1986; Fig. 2).

The "effective strain rate" in the matrix, $\dot{\epsilon}_E$, is defined as

$$\dot{\epsilon}_E = \sqrt{\mathbf{II_D}} = \sqrt{\frac{1}{2}\,\mathrm{trace}\,(\mathbf{DD})} = \sqrt{\frac{1}{2}\,\dot{\epsilon}_{i'j'}\dot{\epsilon}_{i'j'}}, \tag{10}$$

(e.g., Eq. 4.20 in Ranalli, 1995), where $\mathbf{II_D}$ is the second invariant of tensor **D** for incompressible flow. For the case considered here, the effective strain rate for the far-field flow in the matrix is

$$\dot{\epsilon}_E = \sqrt{\dot{\epsilon}_{1'1'}^2 + \dot{\epsilon}_{1'2'}^2} = \sqrt{q^2+s^2}, \tag{11}$$

which corresponds to the magnitude of the principal stretching rates given by the eigenvalues of the rate of deformation tensor **D**, as already established above.

The definition of the kinematic vorticity number W_k (Truesdell, 1953; Means et al., 1980; Jiang, 2010; and many others) is

$$W_k = \sqrt{\frac{-\mathrm{trace}\,(\mathbf{WW})}{\mathrm{trace}\,(\mathbf{DD})}} = \frac{|\mathbf{w}|}{\sqrt{2\,\mathrm{trace}\,(\mathbf{DD})}} = \frac{|\mathbf{w}|}{\sqrt{2\dot{\epsilon}_{i'j'}\dot{\epsilon}_{i'j'}}} = \frac{|\mathbf{w}|}{\sqrt{2\left(\dot{\epsilon}_1^2+\dot{\epsilon}_2^2+\dot{\epsilon}_3^2\right)}} = \frac{|\mathbf{w}|}{2\dot{\epsilon}_E} \tag{12}$$

where $|\mathbf{w}|$ is the magnitude of the vorticity vector, $\mathbf{w} = \mathrm{curl}\ \mathbf{v}$, **v** is the velocity field, and $\dot{\epsilon}_1, \dot{\epsilon}_2, \dot{\epsilon}_3$ are the principal stretching rates parallel to the ISA. W_k lies between 0 (pure shear) and 1 (simple shear) for the range of 2D incompressible flows considered here. For the 2D flow in the matrix, $\mathbf{w} = -2\omega_{1'2'}\mathbf{k}$ (Means et al., 1980), where **k** is the unit vector pointing out of the **ij** plane, containing the $x_{1'}$-$x_{2'}$ and x_1-x_2 axes (Fig. 1). From Eq. (12) above, it follows that W_k in the matrix is

$$W_k = \frac{|\omega_{1'2'}|}{\dot{\epsilon}_E} = \frac{|s|}{\sqrt{q^2+s^2}} = \frac{1}{\sqrt{\left(\frac{q}{s}\right)^2+1}} = \frac{1}{\sqrt{4s_r+1}} \tag{13}$$

or, alternatively,

$$s_r = \frac{1}{2}\sqrt{\frac{1}{W_k^2}-1}. \tag{14}$$

From Eq. (13), the relation of the magnitudes of s and q to the kinematic vorticity number in the matrix W_k, for a given effective strain rate $\dot{\epsilon}_E$, is

$$|s| = \dot{\epsilon}_E W_k \tag{15}$$

$$|q| = \dot{\epsilon}_E\sqrt{1-W_k^2}. \tag{16}$$

For simplicity, $\dot{\epsilon}_E$ in the matrix is always normalized to be 1, but the results can readily be scaled to any natural strain rate. For a given W_k in the matrix, Eq.'s (15) and (16) can be used to determine the magnitudes of q and s and, from Eq. (5), $p = s$. Sign conventions are as introduced above: positive s for dextral shear, positive q for stretch parallel to $x_{1'}$ (i.e., transpression).

For flow within the inclusion, the velocity gradient matrix $\mathbf{L}^{\mathrm{inclusion}}$, rate of deformation tensor $\mathbf{D}^{\mathrm{inclusion}}$, and vorticity tensor $\mathbf{W}^{\mathrm{inclusion}}$ are related by.

$$\mathbf{L}^{\mathrm{inclusion}} = \mathbf{D}^{\mathrm{inclusion}} + \mathbf{W}^{\mathrm{inclusion}} = \begin{bmatrix} \dot{\epsilon}_{11}^{\mathrm{inclusion}} & \dot{\epsilon}_{12}^{\mathrm{inclusion}} \\ \dot{\epsilon}_{12}^{\mathrm{inclusion}} & -\dot{\epsilon}_{11}^{\mathrm{inclusion}} \end{bmatrix} + \begin{bmatrix} 0 & \omega_{12}^{\mathrm{inclusion}} \\ -\omega_{12}^{\mathrm{inclusion}} & 0 \end{bmatrix}. \tag{17}$$

With R as the axial ratio (a/b, Fig. 1) and δ the viscosity ratio of inclusion to matrix, the solutions of Bilby and Kolbuszewski (1977) for the components of Eq. (17) are

$$\dot{\epsilon}_{11}^{\mathrm{inclusion}} = \dot{R}/(2R) = (q\,cos(2\psi) + s\,sin(2\psi))(R+1)^2/J \tag{18}$$

$$\dot{\epsilon}_{12}^{\mathrm{inclusion}} = (s\,cos(2\psi) - q\,sin(2\psi))(R+1)^2/K \tag{19}$$

$$\omega_{12}^{\mathrm{inclusion}} = \dot{\epsilon}_{12}^{\mathrm{inclusion}}\left(R^2+1\right)/\left(R^2-1\right), \tag{20}$$

with

$$J = R^2 + 2\delta R + 1 \tag{21}$$

$$K = \delta R^2 + 2R + \delta. \tag{22}$$

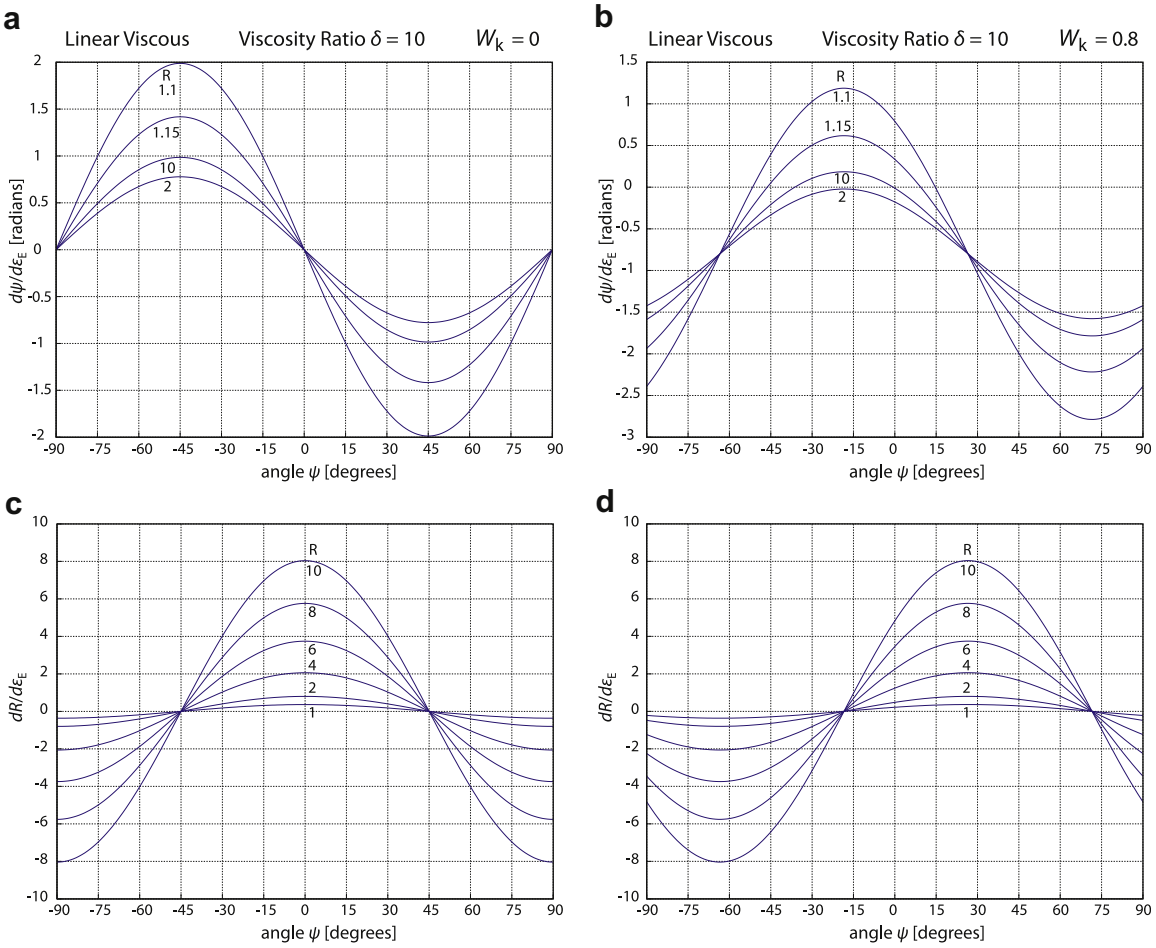

Fig. 2. Normalized rotation rate $d\psi/d\epsilon_E$ and stretching rate $dR/d\epsilon_E$ of an inclusion (where $d\epsilon_E = \dot{\epsilon}_E dt$ for effective strain rate $\dot{\epsilon}_E$ in the matrix), for linear viscous rheology of both inclusion and matrix and viscosity ratio $\delta = 10$. Fig. 2a and c are for pure shear ($W_k = 0$), in which case the orientation for maximum rotation rate is $\psi_1 = -45°$, that for minimum rotation rate is $\psi_2 = 45°$, and the two inflection points in the rotation rate curves are $\psi_3 = \pm 90°$ and $\psi_4 = 0°$; ψ_3 and ψ_4 also correspond to the orientations of the ISA and thus the orientations of minimum and maximum rate of elongation of the inclusion. Fig. 2b and d are for dextral transpression with $W_k = 0.8$. In this case $\psi_1 = -18.4°$, $\psi_2 = 71.6°$, $\psi_3 = -63.4°$ and $\psi_4 = 26.6°$.

The rate of rotation of the inclusion axis x_1 relative to the external axis $x_{1'}$ is

$$\dot{\psi} = (s\,cos(2\psi) - q\,sin(2\psi))(R+1)L/(R-1) - p \tag{23}$$

with

$$L = 1 - 2\delta R/K. \tag{24}$$

The value $-p\,(= -\omega_{1'2'})$ on the right-hand-side (RHS) of Eq. (23) is one half the magnitude of the vorticity vector, which in turn is equal to the rotation rate of lines parallel to the ISA of the far-field matrix flow or the average rotation rate of all lines in this background flow (counter-clockwise positive) (Means et al., 1980). The rest of the expression on the RHS of Eq. (23) is the rate of rotation of the inclusion axis x_1 relative to lines instantaneously parallel to the ISA in the matrix (equivalent to $\dot{\psi} + p$).

Eq.'s (18), (19), and (23) can be rearranged so that the scalar results $\dot{\epsilon}_{11}^{inclusion}$, $\dot{\epsilon}_{12}^{inclusion}$, and $\dot{\psi} + p$ are obtained through the multiplication of two vectors: one vector with components q and s from the rate of deformation tensor **D** describing the imposed matrix deformation and one defining the particle orientation in terms of the direction cosines (as double angles) (cf. Jiang, in press).

$$\frac{\dot{\epsilon}_{11}^{inclusion}}{(R+1)^2/J} = [\,q \quad s\,] \begin{bmatrix} cos(2\psi) \\ sin(2\psi) \end{bmatrix} \tag{25}$$

$$\frac{\dot{\epsilon}_{12}^{inclusion}}{(R+1)^2/K} = [\,s \quad -q\,] \begin{bmatrix} cos(2\psi) \\ sin(2\psi) \end{bmatrix} \tag{26}$$

$$\frac{\dot{\psi} + p}{(R+1)L/(R-1)} = [\,s \quad -q\,] \begin{bmatrix} cos(2\psi) \\ sin(2\psi) \end{bmatrix} \tag{27}$$

This form of the equations demonstrates that, when correctly scaled relative to the axial ratio R and the viscosity ratio δ (included in the scalar terms J, K, and L above), the instantaneous behaviour of all inclusions is described by simple expressions that are dependent only on **D** and the inclusion orientation. The scalar factors on the left-hand-side (LHS) of Eq.'s (25) and (27) both approach 1 as R approaches infinity, regardless of the viscosity ratio δ (provided, in the case of Eq. (25), that it remains finite, i.e. the inclusion is not rigid), whereas for Eq. (26), the scalar factor approaches δ as R approaches infinity. It follows that the RHS's of Eq.'s (25–27) simply describe the behaviour of a passive line ($R = \infty$, $\delta = 1$), with the scaling on the LHS's transforming this into a description of the complete range of inclusion behaviour. In fact, the scalar factors in Eq.'s (25–27) are always 1 for $\delta = 1$, regardless of R, which returns the intuitive result that the behaviour of directions in a passive inclusion is the same as for a passive line. For a rigid inclusion ($\delta = \infty$), the scalar factor in the denominator of the LHS of Eq. (27) is $(R+1)(R-1)/(R^2+1)$ and, for $R = 1$, the rotation rate for all directions is $-p$. In all other cases ($\delta \neq 1$ or ∞), the rotation rate $\dot{\psi}$

for $R = 1$ corresponds to a singularity, because the long axis of a circular inclusion is indeterminate.

The RHS's of the three equations will have zero, maximum and minimum values for the same orientations of the long axis of the inclusion regardless of R and δ, and directly correspond to the case of a passive line. From Eq. (25), the rate of stretch $\dot{\epsilon}_{11}^{\text{inclusion}}$ (and thus $\dot{R}$) for all inclusions is zero when

$$tan(2\psi) = \frac{-q}{s} = -2s_r, \tag{28}$$

corresponding to the directions of no instantaneous stretch of a passive line for the particular flow. The maximum and minimum values of the RHS are $\pm\sqrt{q^2+s^2}$ ($= \pm\dot{\epsilon}_E$; Eq. (11)) and are attained when

$$tan(2\psi) = \frac{s}{q} = \frac{1}{2s_r}, \tag{29}$$

corresponding to the orientation of the ISA. Use of the standard trigonometric identity that $tan(\theta+\frac{\pi}{2}) = -\cot\theta$ immediately establishes from Eq.'s (28) and (29) that the two perpendicular directions of no instantaneous stretch are at 45° to the two perpendicular ISA.

For both Eq.'s (26) and (27), the zero value of the RHS is attained when

$$\tan(2\psi) = \frac{s}{q} = \frac{1}{2s_r}, \tag{30}$$

again corresponding to the orientation of the ISA. By definition, the shear strain rate parallel to the ISA is zero, both for a passive line and, by inference from Eq. (26), for all possible elliptical inclusions in this orientation. From Eq. (27), $\dot{\psi} = -p$ for all inclusions with axes parallel to the ISA, which establishes that in this orientation all inclusions rotate at a rate determined by the vorticity of the imposed 2D flow, i.e. $-p = -\omega_{1'2'} = -\frac{\dot{\gamma}}{2}$. The maximum and minimum values of the RHS of Eq.'s (26) and (27) are again $\pm\sqrt{q^2+s^2}(= \pm\dot{\epsilon}_E)$ and are attained when

$$tan(2\psi) = \frac{-q}{s} = -2s_r, \tag{31}$$

corresponding to the directions of no instantaneous stretch.

In summary, the RHS of Eq. (25) and the RHS common to both Eq. (26) and (27) describe two sinusoidal curves of amplitude $\dot{\epsilon}_E$ that are 45° out of phase with regard to ψ, the curves for Eq. (25) passing through maximum and minimum at the ISA, where the curves for Eq.'s (26) and (27) pass through zero. Plots of the stretching rate $\dot{R}$ and rotation rate $\dot{\psi}$ for all inclusions, regardless of their R and δ values, will be identical if their orientation is plotted relative to the ISA and the ordinate is scaled according to the LHS of Eq.'s (25–27).

Relative to the axes x_1-x_2, the orientations of the ISA within the inclusion are the eigenvectors of $\mathbf{D}^{\text{inclusion}}$ and the eigenvalues give the corresponding principal stretching rates. The effective strain rate within the inclusion is

$$\dot{\epsilon}_E^{\text{inclusion}} = \sqrt{\left(\dot{\epsilon}_{11}^{\text{inclusion}}\right)^2 + \left(\dot{\epsilon}_{12}^{\text{inclusion}}\right)^2}, \tag{32}$$

and the kinematic vorticity number within the inclusion, relative to the inclusion axes x_1-x_2, is

$$W_k^{\text{inclusion}} = \frac{|\omega_{12}^{\text{inclusion}}|}{\dot{\epsilon}_E^{\text{inclusion}}}. \tag{33}$$

From Eq. (20) it is clear that $\omega_{12}^{\text{inclusion}} \to \infty$ as $R \to 1$ and therefore also $W_k^{\text{inclusion}} \to \infty$ as $R \to 1$. The vorticity vector for flow within the inclusion relative to the external axes $x_{1'}$-$x_{2'}$ is

$$\mathbf{w}_{1'2'}^{\text{inclusion}} = 2\left(-\omega_{12}^{\text{inclusion}} + \dot{\psi}\right)\mathbf{k} \tag{34}$$

and from Eq. (8) of Bilby and Kolbuszewski (1977)

$$-\omega_{12}^{\text{inclusion}} + \dot{\psi} = (s\,cos(2\psi) - q\,sin(2\psi))(\delta-1)\left(R^2-1\right)/K - p \tag{35}$$

or, on rearranging,

$$\frac{-\omega_{12}^{\text{inclusion}} + \dot{\psi} + p}{\left(\delta-1\right)\left(R^2-1\right)/K} = \begin{bmatrix} s & -q \end{bmatrix}\begin{bmatrix} cos(2\psi) \\ sin(2\psi) \end{bmatrix}. \tag{36}$$

If required, the kinematic vorticity number within the inclusion relative to the external axes $x_{1'}$-$x_{2'}$ can be determined from Eq.'s (34) and (35) using the definition in Eq. (12),

$$W_k^{\text{inclusion}} = \frac{|\mathbf{w}_{1'2'}^{\text{inclusion}}|}{2\dot{\epsilon}_E^{\text{inclusion}}}. \tag{37}$$

However, as pointed out by Means et al. (1980), it is the value of the vorticity and kinematic vorticity number in Eq. (33) that is more relevant for fabric development within the inclusion.

From Eq. (18) for $\dot{R}$ and Eq. (23) for $\dot{\psi}$, the progressive change, with increasing matrix strain, in the shape and orientation of an inclusion with a specific initial axial ratio and orientation represents an initial value problem for ordinary differential equations (ODE's), which can be solved by standard numerical methods. Plots presented here were generated using routines in MATLAB and the relevant scripts are available in the supplementary material.

3. General principles of inclusion behaviour

Before considering the extension to power-law rheology, it is useful to first summarize general principles that control the behaviour of a 2D inclusion with an elliptical cross-section embedded in an infinite matrix undergoing a general incompressible viscous 2D flow. Most of these observations are in fact independent of the rheology of the inclusion.

(1) For an inclusion with a specific axial ratio R, the pattern of the perturbation velocity field (e.g., Passchier et al., 2005), and therefore the stress, pressure, and strain rate, is only determined by the orientation of the inclusion relative to the far-field ISA in the matrix, although the magnitudes are determined by the (effective) viscosity ratio. The vorticity of the imposed flow has no influence on the distribution of stress, pressure and strain rate relative to the inclusion axes. $\mathbf{L}^{\text{inclusion}}$ only depends on the orientation of the inclusion relative to the ISA and therefore plots of $\dot{R} = dR/dt$ (or $dR/d\epsilon_E$; e.g., Fig. 2c and d), $W_k^{\text{inclusion}}$, and $\dot{\epsilon}_E^{\text{inclusion}}$ are identical, regardless of W_k in the matrix, when plotted for angles relative to the ISA. As developed below, this is also the case for the effective viscosity ratio in power-law viscous materials, which depends on $\dot{\epsilon}_E^{\text{inclusion}}$. This general observation is implicit in the fact that the components of the vorticity tensor in the matrix flow ($p = \omega_{1'2'}$) do not appear in Eq.'s (18–20) for the components of $\mathbf{L}^{\text{inclusion}}$. The rotation rate of the long axis of the inclusion $\dot{\psi} = d\psi/dt$ (or $d\psi/d\epsilon_E$) also does not vary relative to axes instantaneously parallel to the ISA (first term on the RHS of Eq. (23)). However, it does vary relative to the external axes $x_{1'}$-$x_{2'}$, with all curves, regardless of R, being shifted in magnitude

by $-p$ (0 in Fig. 2a, −0.8 in Fig. 2b), as is clear from the presence of this second constant term on the RHS of Eq. (23).

(2) Switching ISA, or the equivalent operations of rotating an inclusion 90° relative to the ISA or inverting the axial ratio R to $1/R$, inverts the sign of the perturbation velocity, the stress (and pressure) and strain rate, but the pattern and absolute magnitudes remain unchanged.

(3) The orientations of maximum and minimum rate of rotation of an isolated inclusion are perpendicular to one another and the orientations corresponding to inflection points in the rotation rate curves bisect the angle between them (Fig. 2a and b). The orientations of maximum and minimum rate of rotation themselves bisect the angles between the eigenvectors of flow. All these orientations depend only on the background flow and not on the axial ratio of the particle, the viscosity ratio or the rheology. They therefore also correspond to the behaviour of a passive line in a homogeneous material (see the discussion after Eq. (27)). Following Ghosh and Ramberg (1976), but allowing for the difference in definition of angles, the orientations ψ_1 for the maximum rate, ψ_2 for the minimum rotation rate, and $\psi_{3,4}$ for the two inflection points are:

$$\psi_1 = -\frac{1}{2}\tan^{-1}(2s_r) \tag{38}$$

$$\psi_2 = \psi_1 + 90^\circ \tag{39}$$

$$\psi_{3,4} = \psi_2 \pm 45^\circ \tag{40}$$

These results are identical to those derived directly from the solutions of Bilby and Kolbuszewski (1977) for a viscous elliptical inclusion (see Eq.'s 28–31 and related discussion above). Note that the terms "maximum and minimum rotation rates" also consider the sign. For example in a general 2D flow with a dextral shear component, the maximum (positive and counter-clockwise) rotation rate will be antithetic to the sense of shear and smaller in absolute magnitude than the minimum (negative and clockwise) rotation rate, which is synthetic to the shear sense (Fig. 2b).

(4) The pattern of the perturbation velocity field (and stress, pressure, strain rate) is symmetric relative to the inclusion axes for orientations $\psi_{1,2,3,4}$. For these orientations, the ISA inside the inclusion are parallel to the ISA in the far-field flow. For orientations $\psi_{3,4}$ (inflection points in rotation rate), the ISA are also parallel to the axes of the inclusion and $W_k^{inclusion} = 0$ (i.e., coaxial deformation). For orientations $\psi_{1,2}$ (maximum and minimum rotation rates), the ISA are at 45° to the inclusion axes, $W_k^{inclusion} \to \infty$ as $R \to 1$ but $W_k^{inclusion} \to 1$ (simple shear) for increasing R and is already close to unity for $R > \sim 5$. For all other orientations, there is a refraction of axes, so that for a more viscous inclusion ($\delta > 1$), the principal axes inside the inclusion are refracted to make an angle closer to 90° to the inclusion interface (Strömgård, 1973; Treagus, 1973; Mancktelow, 1993). This effect becomes more pronounced with increasing R and viscosity ratio δ and is reflected in $W_k^{inclusion}$, which, for larger R and δ, is small for most orientations ("spinning coaxial deformation", cf. Fig. 4c of Lister and Williams, 1983) and only rapidly approaches 1 (simple shear) for a narrow range of orientations around $\psi_{1,2}$.

(5) All inclusions rotate at the same rate at the inflection points (orientations $\psi_{3,4}$) regardless of their axial ratio, effective viscosity ratio or rheology (Fig. 2a and b). This rotation rate has a magnitude equal to $-p = -\omega_{1'2'}$ (0 in Fig. 2a, −0.8 in Fig. 2b), which is also equal to the average rotation rate of all lines in the matrix flow or the average rotation rate of any two perpendicular lines. It follows that it must also be the constant rate of rotation of any circular rigid particle. This behaviour is readily explained when considering that this is also the orientation of the ISA. Any general deformation can be considered in terms of an instantaneous stretch related to the ISA and a rigid body rotation, which can be described by the rotation of the two lines parallel to the ISA which remain instantaneously perpendicular. When the axes of the inclusion are parallel to the ISA, the elongation of the inclusion is coaxial (at a rate determined by the effective viscosity ratio, the rheology and the current axial ratio) and the axes of the inclusion therefore remain fixed to the same material lines (which remain perpendicular). These lines rotate according to the imposed matrix vorticity, irrespective of the effective viscosity ratio, rheology or the current axial ratio. It follows that the rotation rate of all inclusions is the same when the axes are oriented parallel to the ISA, which corresponds to the inflection point in the rotation rate curves.

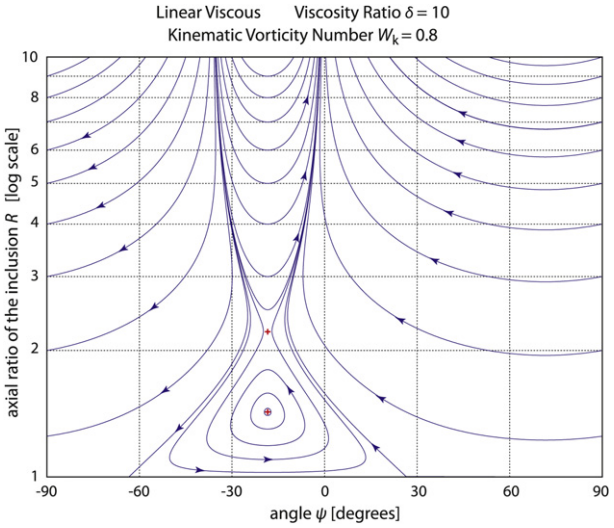

Fig. 3. R-ψ plot for linear viscous rheology, viscosity ratio $\delta = 10$, and dextral transpression with $W_k = 0.8$ (i.e., directly comparable to Fig. 2b and d). There are two stationary points (red crosses) with values of $R = 1.43$ and $R = 2.22$ and corresponding values for $\epsilon_E^{inclusion}$ of 0.177 and 0.163. Both lie on the line of mirror symmetry, which is the orientation $\psi_1 = -18.4^\circ$ of maximum rotation rate and zero stretching rate (cf. Fig. 2b and d). The maximum rotation rate for the two stationary points must be exactly zero (cf. $R = 2$ in Fig. 2b, which is very close to the value $R = 2.22$ for one of the stationary points). For linear viscous rheology and $W_k = 0.8$, a single stationary point occurs for $\delta = 8.4362$; for lesser values, there are no stationary points, for larger values there are always two points (see script "Eq_23_stationary_points" in the supplementary material). (For interpretation of the references to colour in this figure legend, the reader is referred to the web version of this article.)

(6) For orientations of maximum and minimum rotation rate $\psi_{1,2}$, the stretching rate $\dot{R} = dR/dt$ (or $dR/d\epsilon_E$) of an inclusion is always zero (Fig. 2). In these orientations, the angle between the ISA and the inclusion long axis is 45° (both in the inclusion and in the matrix far-field flow) and the inclusion axes thereby correspond to directions of no instantaneous stretch. For orientations with the long axis parallel to $\psi_{3,4}$, the ISA coincide with the axes of the inclusion, the internal deformation within the inclusion is coaxial pure shear and the rate of change in the axial ratio is either a maximum (long axis parallel to stretching axis) or a minimum (long axis parallel to shortening axis).

(7) In R-ψ plots (Fig. 3) showing trajectories with time (or increasing matrix strain) of axial ratio R (ordinate, log scale) and long axis orientation ψ (abscissa), as introduced by Bilby and Kolbuszewski (1977; Figs. 2–5) and subsequently referred to as "phase portraits" (Spence and Wilmott, 1988),

"phase diagrams" (Mulchrone and Walsh, 2006), or "phase-space plots" (Fletcher, 2009), there is reflection symmetry about vertical lines corresponding to the orientations of maximum and minimum rotation rate ($\psi_1 = -18.4°, \psi_2 = 71.6°$ in Fig. 3 with $W_k = 0.8$).

(8) Passive lines rotate away from the shortening eigenvector toward the extending eigenvector. With increasing axial ratio R, all inclusions rotate like a passive marker line, regardless of rheology. It follows that, with increasing R, trajectories in R-ψ space diverge away from the shortening eigenvector ($-36.9°$ in Fig. 3) and toward the extending eigenvector (0° for transpression, Fig. 3).

(9) A deformable inclusion with circular cross-section ($R = 1$) has no long axis (ψ is undefined) but is instantaneously shortened and stretched parallel to the ISA. In R-ψ space, the corresponding trajectory therefore approaches the $R = 1$ limit at ψ angles corresponding to the ISA (i.e., $\psi_{3,4} = -63.4°$ and 26.6° in Fig. 3). All other trajectories are asymptotic to the abscissa at $R = 1$, with the sense in which they approach this asymptote changing to either side of the critical trajectory trending toward points (ψ_3, $R = 1$) and (ψ_4, $R = 1$).

(10) The trajectory plots in R-ψ space are point symmetric around (ψ_3, $R = 1$) and (ψ_4, $R = 1$). Plots extended to the space $R < 1$ (i.e. where ψ is now the angle to the short axis b, Fig. 1), as in Bilby and Kolbuszewski (1977; Figs. 2–5), can be readily generated from plots with $R \geq 1$ (e.g., Fig. 3) by making use of this symmetry.

(11) Laminar viscous flow is reversible. Reversing time reverses both the simple and pure shear components. The example of Fig. 3 for dextral transpression with $W_k = 0.8$ becomes the case of sinistral transtension with the same W_k by simply reversing the sense of the arrows on the trajectories. In physical space, reversing the sense of shear without changing the pure shear component is equivalent to a reflection about either the $x_{1'}$ or $x_{2'}$ axes (Fig. 1), which is the same as changing the sign of ψ, which is in turn the same as a reflection about the vertical $\psi = 0$ line in an R-ψ plot. It follows that the full range of behaviour corresponding to a specific value of W_k can be inferred from a single plot such as Fig. 3.

(12) For deformable linear viscous inclusions in a linear viscous matrix, there are several regimes of behaviour. As discussed by Bilby and Kolbuszewski (1977), the trajectory plots in R-ψ space for pure shear matrix flow are similar for all viscosity ratios δ of inclusion to matrix; inclusions continuously elongate and their long axes asymptotically approach the principal stretching axis of the matrix flow with time (*op. cit.*, Fig. 2). However, for simple shear there are three regimes: (a) for $\delta < 2$, all inclusions elongate indefinitely and asymptotically approach the shear plane (*op. cit.*, Fig. 3); (b) for $2 < \delta < \sim 3.40$ there are two fields of behaviour separated by the critical trajectory passing through $\pm 45°$ (i.e., $\psi_{3,4}$) at $R = 1$; within this bounding trajectory inclusions oscillate around the shear plane, on it and outside it they continuously elongate as their long axes approach the shear plane asymptotically (*op. cit.*, Fig. 4); (c) for $\delta > \sim 3.40$, the shape of all inclusions changes periodically; those within the critical trajectory oscillate in orientation, those outside continuously rotate; an inclusion on the critical trajectory oscillates in orientation – when circular, it stretches parallel to the ISA, then rotates synthetically and stretches to reach a maximum R when parallel to the shear plane, continues to rotate with decreasing R until $R = 1$ as it again reaches the orientation of the ISA, and the cycle repeats (*op. cit.*, Fig. 5). A further regime, (d), which is covered by the general discussion in Bilby and Kolbuszewski (1977) but not explicitly presented in an R-ψ plot, occurs for mixed flow between simple and pure shear. An example is given in Fig. 3 for a viscosity ratio $\delta = 10$ and kinematic vorticity number $W_k = 0.8$. In this case, there are two stationary points, one surrounded by closed trajectories (with $R = 1.43$) and one at a saddle point ($R = 2.22$).

(13) Stationary or invariant points in the R-ψ plots are those for which the axial ratio and orientation of the inclusion do not change. However, it is important to note that there is still internal deformation within the inclusion – in Fig. 3, for the case with $R = 1.43$ the effective strain rate in the inclusion is 0.177, for $R = 2.22$ it is 0.163 (for a matrix flow with an effective strain rate of 1). The inclusion axes remain of constant length because they correspond to directions of no instantaneous stretch (see above). As also discussed above, inclusions for which R is instantaneously unchanging always have an orientation $\psi_{1,2}$. However, for stationary points the rotation rate of the long axis must also be zero, and this is only possible if the rotation rate at ψ_1 (for dextral shear) or ψ_2 (for sinistral shear) has an antithetic sense for some values of R (in Fig. 3, for $R < 1.43$ or $R > 2.22$ at $\psi_1 = -18.4°$). R values of the stationary points can be found as the roots of Eq. (49) of Bilby and Kolbuszewski (1977), or numerically (or graphically) as the zero intercepts of the curve of Eq. (23) for rotation rate versus axial ratio R, for the given angle ψ_1 (or ψ_2).

(14) As R increases, the effective strain rate in the inclusion for orientations $\psi_{3,4}$ (with inclusion axes parallel to the ISA) approaches that of the matrix – in this case, the limit is constant strain rate in inclusion and matrix and different magnitudes of stress reflecting the viscosity ratio. For inclusions with axes parallel to $\psi_{1,2}$, which are directions of no stretch but maximum shear stress, the stress will be same in inclusion and matrix but the strain rate will be different, again directly reflecting the viscosity ratio.

4. Power-law viscous rheology

Provided the matrix is linear viscous, the stress and strain rate within an ellipsoidal inclusion is homogeneous. Roscoe (1967), Goddard and Miller (1967), Bilby and Kolbuszewski (1977), and Schmid and Podladchikov (2003) all noted that analytical solutions for a linear viscous inclusion could therefore be extended to the case of an inclusion with more general mechanical properties, but explicit examples were not developed. Gilormini and Montheillet (1986), Gilormini and Germain (1987) and Schmid et al. (2004) did consider power-law viscous rheology, but only for the specific case of pure shear where the axes of the inclusion were parallel to the principal axes. Here the 2D solution of Bilby and Kolbuszewski (1977) is extended to the case of a power-law viscous inclusion. It should be emphasized that the rheology of the inclusion does not affect the overall solution. If an instantaneous effective viscosity ratio is determined, this value can be substituted back into the general solutions of Bilby and Kolbuszewski (1977), Schmid and Podladchikov (2003), or Jiang (2007b, in press) to immediately determine the full velocity field, strain rate, stress, and pressure in both the inclusion and matrix. The progressive change in shape and orientation of the inclusion can also be readily determined, using standard ODE methods, as in the linear case considered above.

For a power-law viscous material, the effective viscosity is given by

$$\mu_{\text{eff}} = \mu_0 \left(\frac{\dot{\epsilon}_E}{\dot{\epsilon}_E^0} \right)^{\frac{1}{n}-1} \tag{41}$$

where μ_0 is the reference viscosity at the reference strain rate $\dot{\epsilon}_E^0$, the effective strain rate is defined in Eq. (10), and n is the power-law stress exponent (e.g., Schmalholz et al., 2008; Deubelbeiss et al., 2010; Mancktelow and Pennacchioni, 2010b). It follows that the effective viscosity ratio $\delta_{eff} = \mu_i/\mu_m$, where μ_i is the effective viscosity in the inclusion and μ_m is the effective viscosity in the matrix, is given by

$$\delta_{eff} = \delta_0 \left(\frac{\dot{\epsilon}_E^{inclusion}}{\dot{\epsilon}_E^0} \right)^{\frac{1}{n_i}-1} \left(\frac{\dot{\epsilon}_E^0}{\dot{\epsilon}_E} \right)^{\frac{1}{n_m}-1}, \quad (42)$$

where $\delta_0 = \frac{\mu_i^0}{\mu_m^0}$ is the effective viscosity ratio at the reference strain rate (i.e., $\dot{\epsilon}_E^{inclusion} = \dot{\epsilon}_E = \dot{\epsilon}_E^0$). Here, the matrix is always considered linear viscous, so that $n_m = 1$ and Eq. (42) reduces to

$$\delta_{eff} = \delta_0 \left(\frac{\dot{\epsilon}_E^{inclusion}}{\dot{\epsilon}_E^0} \right)^{\frac{1}{n_i}-1}. \quad (43)$$

The effective strain rate within the inclusion is still given by Eq.'s (18), (19) and (32) above but now, for a power-law viscous inclusion, using modified versions of Eq.'s (21) and (22):

$$J = R^2 + 2\delta_{eff}R + 1. \quad (44)$$

$$K = \delta_{eff}R^2 + 2R + \delta_{eff}. \quad (45)$$

Eq. (24) also changes to

$$L = 1 - 2\delta_{eff}R/K. \quad (46)$$

For simplicity and without loss of generality, the effective strain rate in the matrix is scaled to unity and the parameter δ_0 defined for this reference unit strain rate (i.e., for $\dot{\epsilon}_E^{inclusion} = \dot{\epsilon}_E = \dot{\epsilon}_E^0 = 1$). This value δ_0 is used as an initial value for δ_{eff} in Eq.'s (44) and (45) to calculate the strain rate components in the inclusion with Eq.'s (18) and (19). A new value of $\dot{\epsilon}_E^{inclusion}$ is calculated from Eq. (32), which is then used to calculate a new value of δ_{eff} with Eq. (43). This process is iterated until δ_{eff} converges (rapidly) to a predefined tolerance. The MATLAB script is available in the supplementary material.

If the matrix also has a power-law viscous rheology, this iterative, semi-analytical approach is no longer appropriate. Numerical finite-element modelling (FEM) can be used, again employing an iterative approach, where, for each iteration, the current calculated effective strain rate at the integration points is used to determine an effective viscosity using Eq. (41). This approach is summarized, for example, in the appendix of Schmalholz et al. (2008). Comparing FEM results for a power-law viscous inclusion in a linear viscous matrix with the semi-analytical results provides an internal check on the numerical models.

5. Results

The major difference for power-law viscous inclusions is that the effective viscosity ratio is a function of the strain rate within the inclusion and therefore varies with axial ratio and orientation. Fig. 4 shows two examples calculated for dextral simple shear ($W_k = 1$), with $\delta_0 = 2$, $R = 1, 2, 3, 4, 6, 8$, and $n_i = 3$ (Fig. 4a) or $n_i = 6$ (Fig. 4b). These plots are mirror symmetric about the orientations of maximum and minimum rotation rates ($\psi_{1,2} = 0°, \pm 90°$), as expected from general point (7) above. The variation in effective viscosity ratio increases with axial ratio and the highest effective viscosity ratio occurs for $\psi_{1,2}$ (at 0°, ±90° for simple shear), which are the directions of no instantaneous stretch of a passive line. As noted above, the behaviour of an inclusion approaches that of an infinite layer or line as $R \to \infty$. For directions parallel to the ISA ($\psi_{3,4} = \pm 45°$ for simple shear), the effective strain rate in the inclusion approaches that of the matrix as $R \to \infty$ and therefore $\delta_{eff} \to \delta_0$ (Fig. 4). For $\psi_{1,2}$ the stretching rate parallel to the axes of the inclusion is zero, so that $\dot{\epsilon}_E^{inclusion} \to \dot{\epsilon}_{12}^{inclusion} \to (1/\delta_{eff})\dot{\epsilon}_E$ as $R \to \infty$. Substituting this result into Eq. (43) for the case, as generally assumed here, that δ_0 is defined for the same strain rate as the far-field flow in the matrix, returns the result that $\delta_{eff} \to (\delta_0)^{n_i}$ as $R \to \infty$. For $R = 1$, $\dot{\epsilon}_E^{inclusion} = [2/(1 + \delta_{eff})]\,\dot{\epsilon}_E$. Substituting into Eq. (43) and rearranging, for $\dot{\epsilon}_E^0 = \dot{\epsilon}_E = 1$, gives:

$$\frac{\delta_{eff}}{\delta_0} = \left(\frac{2}{1 + \delta_{eff}} \right)^{\frac{1}{n_i}-1}, \quad (47)$$

or

$$\delta_{eff} \left(\frac{2}{1 + \delta_{eff}} \right)^{1-\frac{1}{n_i}} - \delta_0 = 0. \quad (48)$$

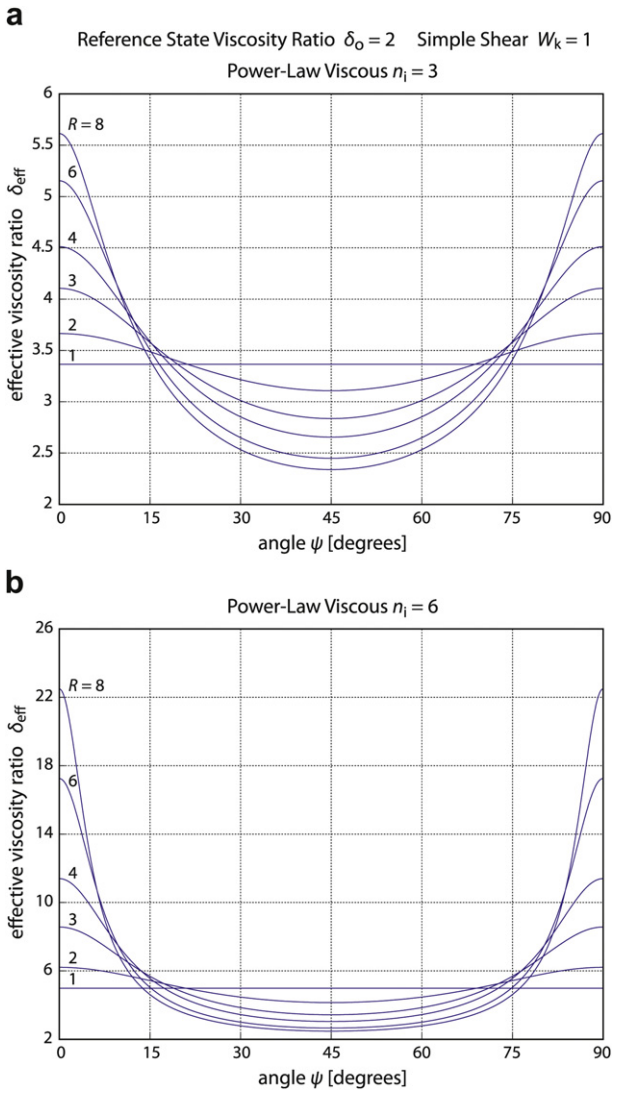

Fig. 4. Variation of the effective viscosity ratio δ_{eff} with orientation ψ and axial ratio R for dextral simple shear, viscosity ratio at reference state $\delta_0 = 2$, linear viscous matrix and stress exponent in the power-law viscous inclusion of a) $n_i = 3$ and b) $n_i = 6$. For a circular inclusion, $\delta_{eff} = 3.37$ in a) and 4.99 in b).

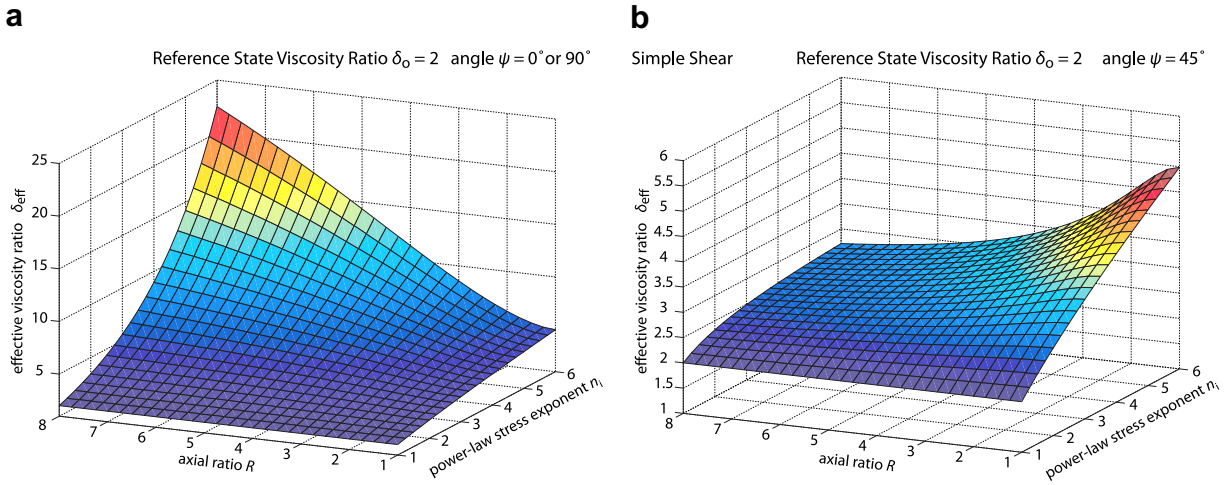

Fig. 5. Variation of effective viscosity ratio δ_{eff} as a function of axial ratio R and power-law stress exponent in the inclusion, n_i, for a viscosity ratio at reference state $\delta_0 = 2$ and a linear viscous matrix undergoing dextral simple shear. a) is for $\psi = 0^\circ$ or $\pm 90^\circ$, b) is for $\psi = 45^\circ$.

These equations do not return a simple analytical solution for δ_{eff} but they can be readily solved numerically or graphically (e.g., by plotting the LHS of Eq. (48) against δ_{eff} to determine the zero intercept, see scripts for "Equation_48" in the Supplementary material). Obviously, for a circular inclusion, the effective strain rate in the inclusion and thus the effective viscosity ratio cannot vary with orientation. For a circular power-law viscous inclusion embedded in a linear viscous matrix with $\delta_0 = 2$, as in Fig. 4, $\delta_{eff} = 3.37$ for $n_i = 3$ (Fig. 4a) and $\delta_{eff} = 4.99$ for $n_i = 6$ (Fig. 4b).

Three-dimensional plots of the effective viscosity ratio for dextral simple shear, $\delta_0 = 2$, R covering the range 1–8, and n_i the range 1–6, are given in Fig. 5a for orientations of the inclusion long axis at $\psi_{1,2} = 0^\circ$ or $\pm 90^\circ$ (i.e. orientations with the maximum effective viscosity ratio; Fig. 4) and in Fig. 5b for $\psi_{3,4} = \pm 45^\circ$ (parallel to the ISA and thus with the maximum particle elongation rate and minimum effective viscosity ratio; Fig. 4). These plots emphasize that, for power-law viscous rheology of the inclusion, the effective viscosity ratio depends strongly on the power-law stress exponent, the axial ratio and the inclusion orientation.

Despite this marked variation in effective viscosity ratio, the behaviour of an isolated viscous inclusion is not fundamentally changed. Comparing the R-ψ plot of Fig. 6 for a power-law viscous inclusion with $n_i = 3$ to the analogous linear viscous case of Fig. 3, it is apparent that the general form is very similar. The major difference is that a power-law viscous inclusion with $\delta_0 > 1$ behaves as if it was markedly more viscous than in the corresponding linear viscous

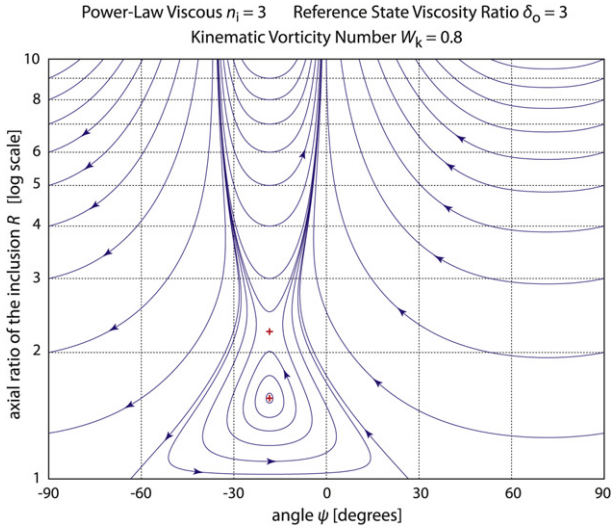

Fig. 6. R-ψ plot directly comparable to Fig. 3 for dextral transpressive shear with $W_k = 0.8$, except that in this case the inclusion has a power-law rheology with $n_i = 3$ and a viscosity ratio at reference state $\delta_0 = 3$. Note the general form is very similar to the linear viscous case of Fig. 3, where $\delta = 10$. There are two stationary points marked with red crosses, one with $R = 1.56$, $\delta_{eff} = 8.98$, and $\dot{\epsilon}_E^{inclusion} = 0.193$; the other with $R = 2.24$, $\delta_{eff} = 10.22$, and $\dot{\epsilon}_E^{inclusion} = 0.159$. For $W_k = 0.8$ and $n_i = 3$, a single stationary point occurs for $\delta_0 = 2.8695$; for lesser values, there are no stationary points, for larger values there are always two points (see script "Equation_23_stationary_points" in the supplementary material). (For interpretation of the references to colour in this figure legend, the reader is referred to the web version of this article.)

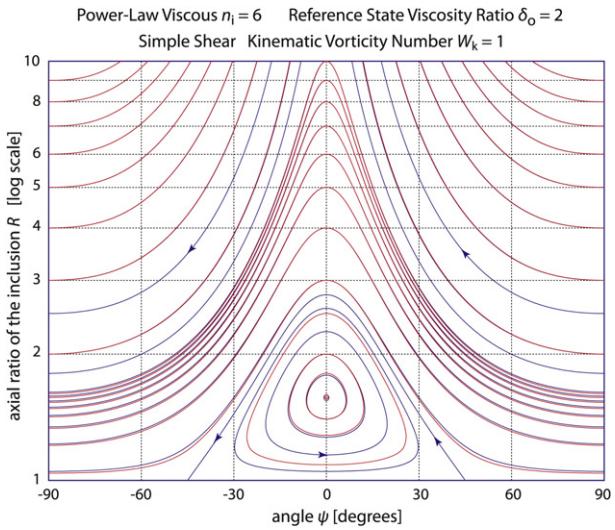

Fig. 7. R-ψ plot for a power-law viscous inclusion with viscosity ratio at reference state $\delta_0 = 2$, a stress exponent $n_i = 6$, a linear viscous matrix, and dextral simple shear. The single stationary point has $R = 1.57$, $\delta_{eff} = 5.48$, and $\dot{\epsilon}_E^{inclusion} = 0.298$. The blue trajectories with arrows are calculated with the semi-analytical solution. The red trajectories without arrows represent streamlines fitted with MATLAB to the FEM results for $d\psi/d\epsilon_E$ and $dR/d\epsilon_E$ values calculated across a grid of discrete R and ψ values. The correspondence is close to perfect: where only one colour trajectory is visible, the corresponding trajectory is either covered or was not calculated. (For interpretation of the references to colour in this figure legend, the reader is referred to the web version of this article.)

case: the example in Fig. 6 with $n_i = 3$ and a reference state viscosity ratio of $\delta_0 = 3$ is comparable to the linear viscous example in Fig. 3 with $\delta = 10$. This is reflected in the values associated with the stationary points in Fig. 6: (1) $R = 1.56$, $\delta_{eff} = 8.98$, and (2) $R = 2.24$, $\delta_{eff} = 10.22$. As noted previously, the behaviour of an elliptical particle in a linear viscous matrix depends on δ_{eff} (together with R, ψ, and W_k), regardless of whether the actual rheology is linear or power-law viscous. R-ψ plots for a linear viscous inclusion and matrix with each of these values of the viscosity ratio δ would have stationary points at exactly corresponding positions. In the linear viscous case, there is obviously only one value of δ, irrespective of axial ratio or orientation, so it is not possible to have a single linear R-ψ plot that can produce the positions of both stationary points in Fig. 6. However, the difference between $\delta_{eff} = 8.98$ and $\delta_{eff} = 10.22$ is not large, so that the example in Fig. 3 with $\delta = 10$ is very similar to Fig. 6, even if it must be different in detail. The important point is that the similarity is for a significantly higher viscosity ratio than the reference state viscosity ratio of $\delta_0 = 3$.

This is again emphasized in Fig. 7, which is an R-ψ plot for simple shear ($W_k = 1$), $\delta_0 = 2$, and $n_i = 6$. The trajectories indicate that all inclusions rotate or oscillate, which for linear viscous behaviour would only occur for $\delta > \sim 3.40$. The single stationary point is developed at $R = 1.57$, with $\delta_{eff} = 5.48$. Once again, R-ψ plots for linear and power-law inclusions are similar in their general form, but with an increased effective viscosity ratio for the power-law viscous example (if $\delta_0 > 1$). However, simply taking a higher value of δ and using the linear viscous solution does not capture the true behaviour, because it cannot reproduce the variation in effective viscosity ratio as a function of R and ψ (Figs. 4 and 5).

The iterative semi-analytical approach used above for a power-law viscous inclusion in a linear viscous matrix is no longer appropriate when the matrix is also power-law viscous. Here a personally-developed finite-element code (e.g., Mancktelow, 2008) is employed to study the effects of a power-law viscous matrix. To produce the R-ψ plots presented as examples here, numerical experiments considered a range of R from 1 to 10 and ψ from 0° to 90°. Examples were calculated for simple shear ($W_k = 1$), with a shear strain rate of 2, corresponding to $\dot{\epsilon}_E^{matrix} = 1$. A mixed pressure-velocity formulation employing a disordered triangular mesh, with 7-node, higher order interpolation for velocity and 3-node linear interpolation for pressure (discontinuous from element to element), was used. The mesh was strongly refined toward the inclusion and one set of nodes always tracked the inclusion interface. At each step, a best-fit ellipse was calculated through the nodal points on the inclusion interface to determine the axial ratio R and orientation ψ. For each initial R-ψ pair, values of R and ψ were recorded for ten time (or ϵ_E) steps of size 0.001 (in later models it was found that 3–4 are actually more than

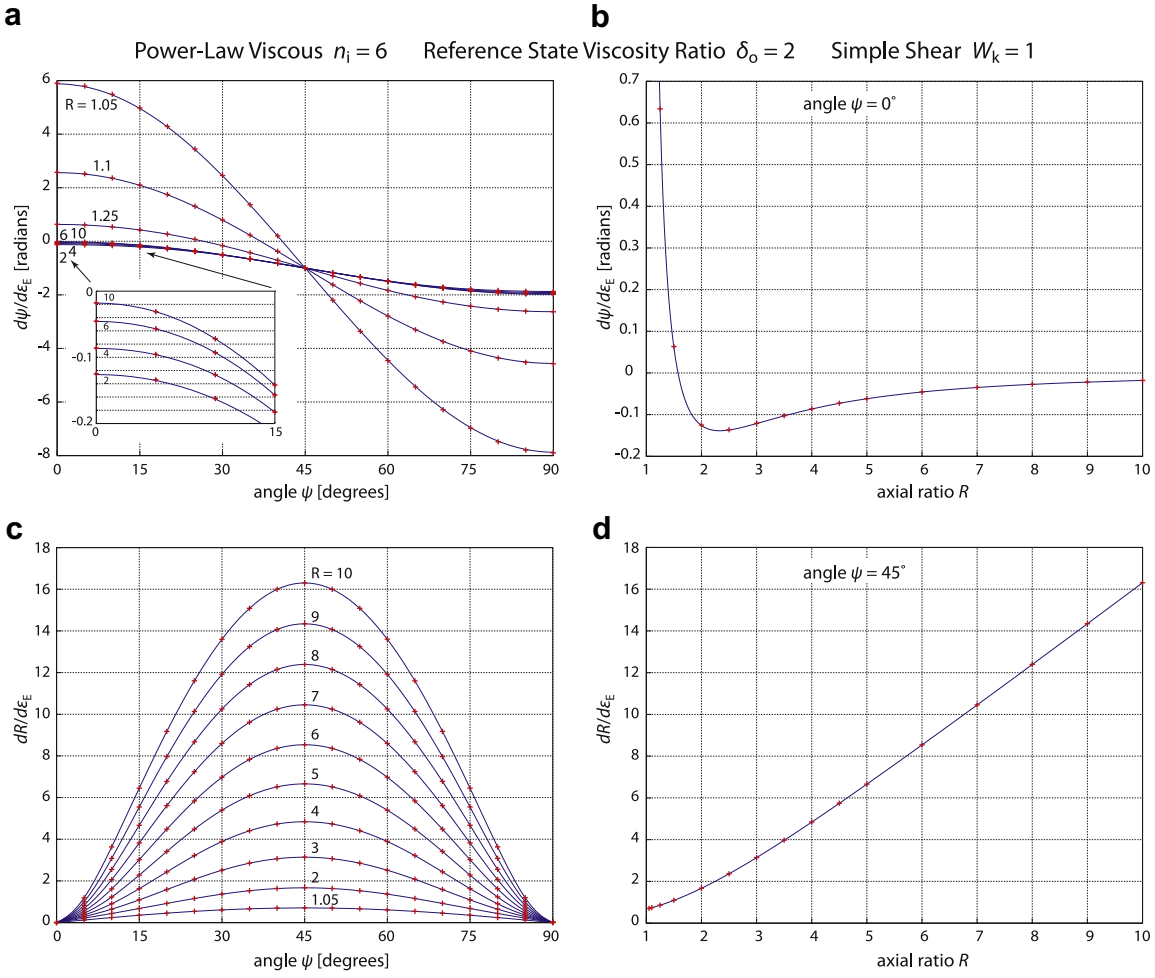

Fig. 8. Comparison of FEM numerical results with the semi-analytical iterative solution for the same model parameters as in Fig. 7. The inset in Fig. 8a is an enlargement of the plots for $R = 10$, 6, 4 and 2 with ψ values from 0 to 15°, details of which are otherwise not discernible in the main plot. In Fig. 8b, the point where the curve for the rotation rate $d\psi/d\epsilon_E$ crosses the zero ordinate (no rotation) corresponds to the stationary point in Fig. 7, with axial ratio $R = 1.57$.

sufficient). A smoothed spline curve fitted to these values of R and ψ with increasing matrix strain ϵ_E allowed the gradients $dR/d\epsilon_E$ and $d\psi/d\epsilon_E$ to be determined at the initial value ($\epsilon_E = 0$).

As can be seen from Figs. 7 and 8, there is excellent correspondence between the results from the finite-element models and the theoretical results for power-law inclusions in a linear viscous matrix. This provides independent control on the accuracy of the numerical models. In Fig. 8, the normalized rotation rate $d\psi/d\epsilon_E$ and elongation rate $dR/d\epsilon_E$ are plotted, as a function of the orientation ψ and axial ratio R, for a power-law viscous inclusion with $\delta_0 = 2$ and $n_i = 6$ in a linear viscous matrix deformed in dextral simple shear. The solid curves represent the semi-analytical solution developed above and the crosses are the results from the corresponding finite-element model. Consistent with the results of Figs. 6 and 7, it can be seen from Fig. 8a that the power-law viscous rheology of the inclusion does not affect the general shape of the rotation-rate curves. However, it does markedly change the magnitudes compared to linear viscous behaviour. As noted above, increasingly elongate inclusions always approach the rotational behaviour of a passive line regardless of rheology and this limit is clear in Fig. 8a. Orientations corresponding to the maximum and minimum rotation rates ($\psi_{1,2} = 0°, \pm 90°$) are always ones of no particle elongation ($dR/d\epsilon_E = 0$) and the effective viscosity in these orientations is at a maximum, with $\delta_{eff} \rightarrow (\delta_0)^{n_i}$ as $R \rightarrow \infty$ (see above). As shown in Fig. 8c, there is consequently a region around $\psi_{1,2}$ (at $0°, \pm 90°$) where the elongation rate of the inclusion is low compared to the linear viscous case, and this effect becomes more marked as the axial ratio R increases.

Power-law viscous rheology in the matrix further increases the contrast in effective viscosity between inclusion and matrix. For a stronger inclusion, the lower strain rate in the inclusion must be compensated by a higher strain rate in the adjacent matrix. Lower strain rate in the inclusion results in a higher effective viscosity and higher strain rate in the matrix in a lower effective viscosity, so the effective viscosity ratio is further increased relative to a linear viscous matrix. For a weaker inclusion, the arguments are reversed. However, the fundamental behaviour, as seen in the R-ψ plot of Fig. 9, is again not dramatically changed. Fig. 9a is similar to Fig. 7 so that, broadly speaking, for $\delta_0 = 2$, a power-law viscous inclusion with a stress exponent $n_i = 3$ in a matrix with a stress exponent $n_m = 3$ behaves like a power-law viscous inclusion with a stress exponent $n_i = 6$ in a linear viscous matrix. Comparing Fig. 7 with Fig. 9b, which were determined for similar parameters except that in Fig. 7 the matrix is linear viscous and in Fig. 9b it is power-law viscous with $n_m = 3$, emphasizes the observation that a power-law viscous matrix produces an effectively stiffer behaviour of the inclusion.

For a power-law viscous matrix, the stress and strain (or strain rate) in the inclusion are no longer strictly homogeneous, but in general the heterogeneity induced is small. For stronger inclusions, the elliptical shape is effectively maintained (Fig. 10a). For weaker inclusions, the shape is indeed modified away from a perfect ellipse as the inclusion becomes highly elongated, producing a more sigmoidal form (Fig. 10b), but the difference is not dramatic.

6. Discussion

Dispersed inclusions in rocks, such as pebbles in conglomerates or ooids in limestones, are often used as markers to determine strain (e.g. Hanna and Fry, 1979; Ramsay and Huber, 1983; Treagus and Treagus, 2002; and many others). The most widespread approach based on inclusion shape is the so-called R_f/ϕ method (e.g., Ramsay, 1967; Dunnet, 1969; Ramsay and Huber, 1983; Lisle, 1985), which accounts for variation in original axial ratio of elliptical particles but assumes passive behaviour. Plots directly

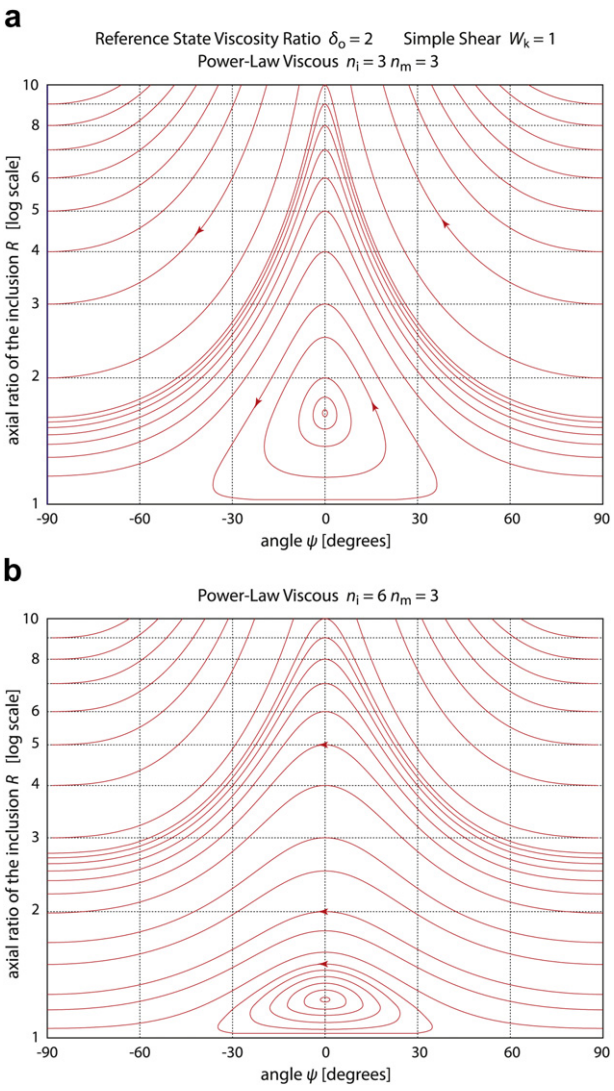

Fig. 9. R-ψ plot determined as streamlines fitting the grid of $d\psi/d\epsilon_E$ and $dR/d\epsilon_E$ values calculated by FEM. a) for $n_i = 3$, $n_m = 3$, and $\delta_0 = 2$; the single stationary point has $R = 1.65$; a stationary point with this R value would develop in a linear viscous system for a viscosity ratio $\delta = 5.09$; b) for $n_i = 6$, $n_m = 3$, and $\delta_0 = 2$; the single stationary point has $R = 1.23$; a stationary point with this R value would develop in a linear viscous system for a viscosity ratio $\delta = 10.58$.

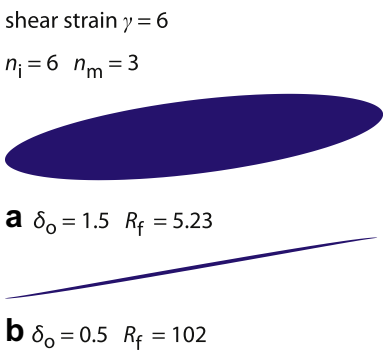

Fig. 10. Shapes of inclusions with an initial circular cross-section ($R_i = 1$) after a dextral simple shear strain of $\gamma = 6$, for a power-law viscous case with $n_i = 6$ and $n_m = 3$ (Mancktelow and Pennacchioni, 2010a, b). In a) the value of the viscosity ratio at reference state is $\delta_0 = 1.5$, and the final axial ratio $R_f = 5.23$, in b) $\delta_0 = 0.5$, and the final axial ratio $R_f = \sim 102$. The axial ratio of a passive circular inclusion would have been 37.97. Note that the shape of the less elongate inclusion in a) is still effectively elliptical, whereas the strongly elongate inclusion in b) has become slightly sigmoidal.

comparable to R_f/ϕ plots can be generated from R-ψ trajectory plots such as Figs. 3, 6 and 7 and 9 by determining the final R_f and orientation ψ_f after a certain time (or imposed matrix strain) of an inclusion of known initial R_i and ψ_i using standard initial value ODE methods (e.g., Jiang, 2007b, in press). For a linear viscous matrix (Fig. 11), the stretching and rotation rates are calculated at each step with Eq.'s (18) and (23), respectively. For a power-law viscous matrix (Fig. 12), the appropriate rates are interpolated from the dense grid of values determined from the finite-element models, based on the same values that were used to generate the trajectories of Fig. 9. Figs. 11 and 12 were both determined for a strain ellipse in the matrix with axial ratio $R_s = 10$.

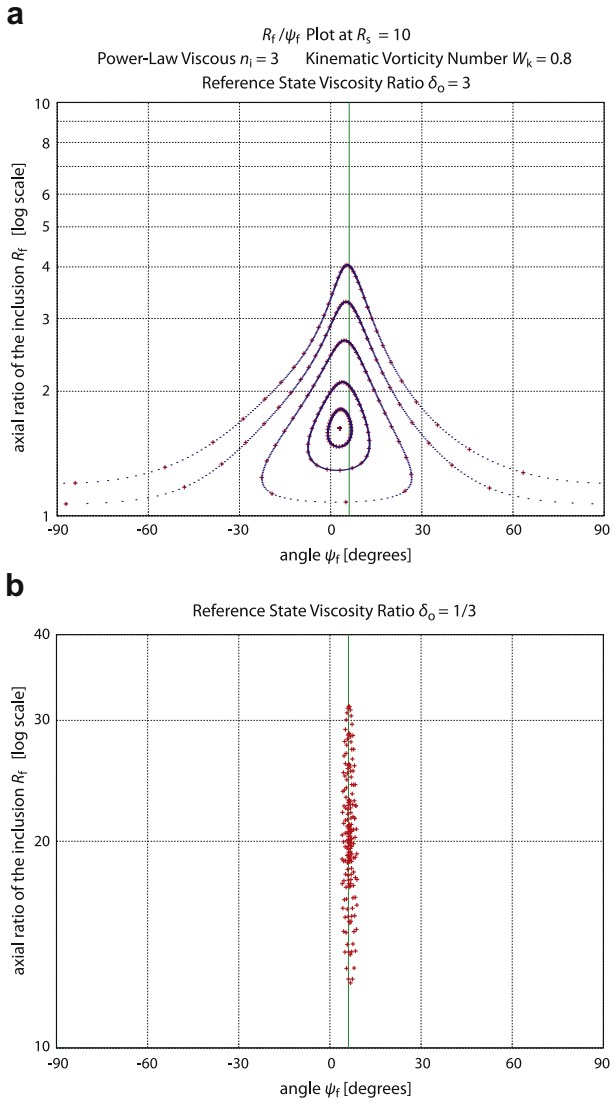

Fig. 11. Plot of the final axial ratio R_f against final orientation ψ_f, which is equivalent to an R_f/ϕ plot as used to determine natural finite strain from a population of elliptical particles measured in 2D. The plots are calculated using the iterative semi-analytical solution for dextral transpression with $W_k = 0.8$ (cf. Fig. 6) at a value for the strain ellipse in the matrix of $R_s = 10$. The long axis of this strain ellipse makes an angle of 6.1° to the shear direction, as indicated by the vertical green line. Results are presented for initial axial ratios R_i of 1, 1.1, 1.25, 1.5, 1.75, and 2; crosses are for 5° intervals in initial orientation from −90 to +90; dots mark intermediate 0.5° intervals in the same range. a) reference state viscosity ratio $\delta_0 = 3$ (i.e. parameters are the same as in Fig. 6); final axial ratio of an initially circular inclusion is $R_f = 1.63$; b) the viscosity ratio is inverted with $\delta_0 = 1/3$; final axial ratio of an initially circular inclusion is $R_f = 19.9$. (For interpretation of the references to colour in this figure legend, the reader is referred to the web version of this article.)

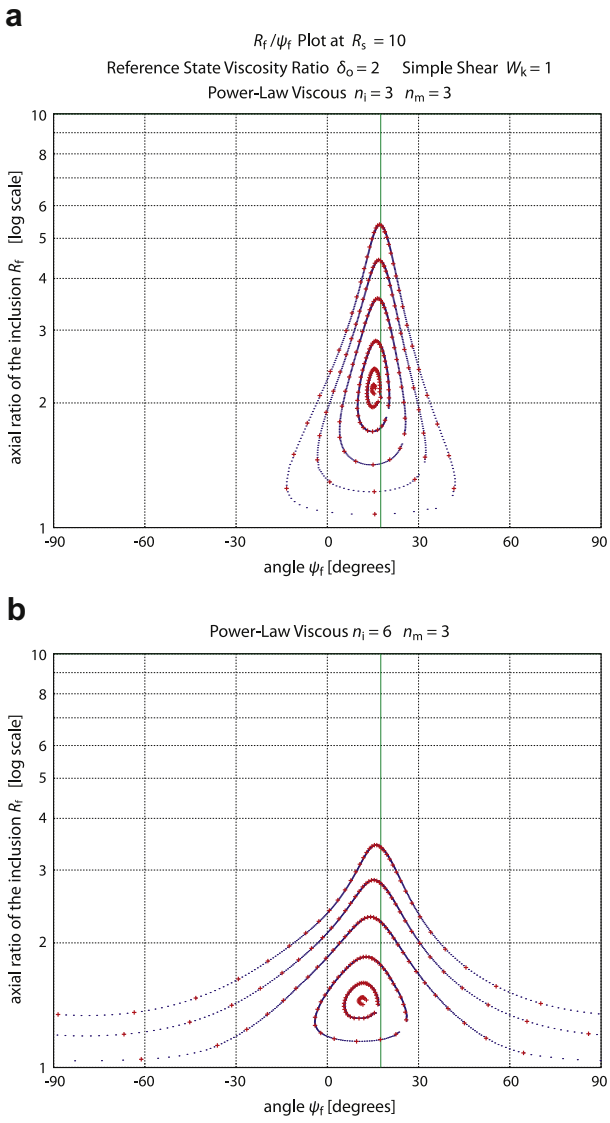

Fig. 12. Plot of the final axial ratio R_f against final orientation ψ_f, derived from the FEM numerical experiments for dextral simple shear with $\delta_0 = 2$ (cf. Fig. 9). Results are presented for a strain ellipse axial ratio in the matrix of $R_s = 10$, for which the long axis of the strain ellipse would make an angle of 17.6° with the shear direction (green vertical line) and for initial axial ratios R_i of 1.02, 1.1, 1.25, 1.5, 1.75, and 2; crosses are for 5° intervals in initial orientation from −90 to +90; dots mark intermediate 0.5° intervals in the same range. a) $n_i = 3$ and $n_m = 3$; final axial ratio of an initially circular inclusion is $R_f \sim 2.15$; b) $n_i = 6$ and $n_m = 3$; final axial ratio of an initially circular inclusion is $R_f \sim 1.45$. Missing values in the bottom right of the closed curves represent inclusions that have passed through or very close to $R = 1$ during their evolution; the lack of a defined orientation ψ and effectively infinite rotation rates of the inclusion axes when $R = 1$ makes interpolation through this singularity using the R-ψ trajectories inaccurate and these values are omitted from the plot. (For interpretation of the references to colour in this figure legend, the reader is referred to the web version of this article.)

Fig. 11 was calculated for the same matrix flow as in Fig. 6, that is for dextral transpression with $W_k = 0.8$. For $R_s = 10$, the long axis of the strain ellipse makes an angle of 6.1° with the shear plane, as indicated by the vertical line. In Fig. 11a, the reference state viscosity ratio is $\delta_0 = 3$ (i.e. parameters are the same as in Fig. 6) and the final axial ratio of an initially circular inclusion is $R_f = 1.63$, whereas in Fig. 11b the viscosity ratio is inverted with $\delta_0 = 1/3$ and the final axial ratio of an initially circular inclusion is $R_f = 19.9$. Fig. 12 presents results where the matrix is also power-law viscous, with $n_m = 3$. The results are for dextral simple shear at $R_s = 10$, for which the long axis of the strain ellipse makes an angle of 17.6°

with the shear plane. The parameters of Fig. 12a correspond to those of Fig. 9a ($\delta_0 = 3$, $n_i = 3$, $n_m = 3$) and those of Figs. 12b to 9b ($\delta_0 = 3$, $n_i = 6$, $n_m = 3$). The plots in Figs. 11 and 12 highlight how results can be markedly different for only rather small differences in reference state viscosity ratios between clast and matrix. This is especially the case for power-law viscous rheology with stress exponents in the range from 3 to 6, as seems appropriate for natural rocks. In particular, when both inclusion and matrix have a power-law rheology, there is a strong positive feedback reflecting the different effective strain rates in the inclusion and adjacent matrix. As a result, the final axial ratio R_f of the non-passive clasts, even for very low reference state viscosity ratios (e.g. 2 in Fig. 12), is very different from the strain ellipse R_s. In Fig. 12b, $R_s = 10$ but R_f for an initially circular inclusion is only ~1.45; even those inclusions with an initial axial ratio $R_i = 2$ never attain values of $R_f > \sim 3.5$. The opposite applies for initially slightly weaker inclusions, which become strongly aligned in the foliation plane and much more elongate than R_s, as can be seen from Fig. 11b. It follows that clasts showing only a small range of rheological behaviour differing slightly from the matrix can show markedly different elongation behaviour, from nearly equant with a wide range of orientations, to tightly aligned and strongly stretched. Establishing the matrix R_s from a population of clasts showing comparable behaviour in nature is unfortunately not really feasible.

The examples of Figs. 11 and 12 are for moderate strain and preserve the typical form of an R_f/ϕ plot. However, as can be seen from Fig. 13 for dextral simple shear, calculated using the semi-analytical solution with $\delta_0 = 3$, $n_i = 3$, and $n_m = 1$, this form breaks down as the shear strain increases. Three points are important to note from this figure: (1) even for the enormous R_s associated with a shear strain of $\gamma = 100$ (Fig. 13d), many inclusions have maintained a low axial ratio ($R_f < 3$) and the complete range in possible orientations, i.e. $-90° \leq \psi_f \leq 90°$; (2) very elongate particles ($R_f > \sim 20$) are tightly oriented very close to the long axis

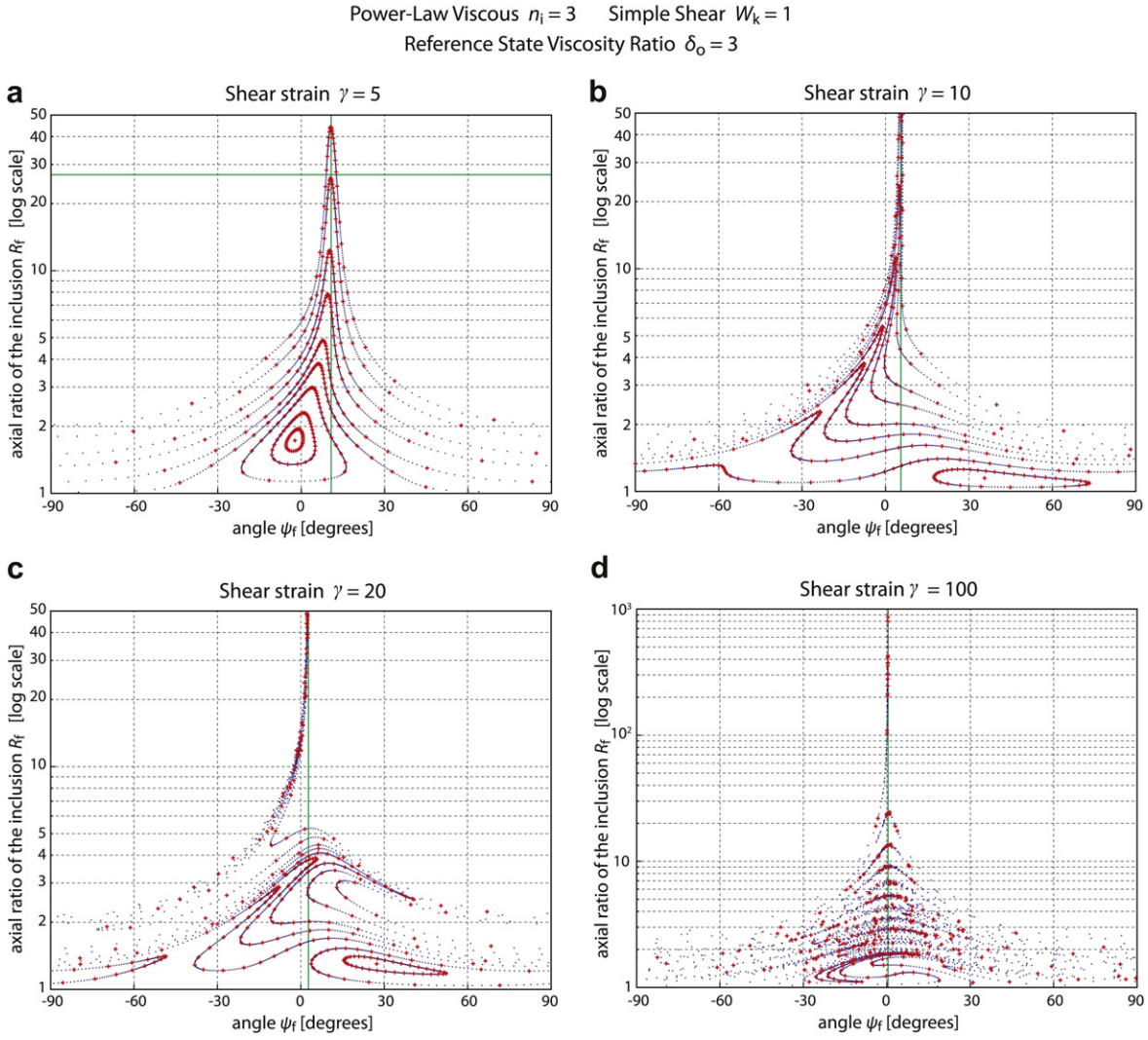

Fig. 13. Plot of the final axial ratio R_f against final orientation ψ_f, using the iterative semi-analytical solution with $\delta_0 = 3$, the power-law exponent in the inclusion $n_i = 3$, and a linear viscous matrix deforming in dextral simple shear. Results are presented for initial axial ratios R_i of 1, 1.1, 1.25, 1.5, 1.75, 2, 2.5, 3, 4, and 5; crosses are for 5° intervals in initial orientation from −90 to +90; dots mark intermediate 0.5° intervals in the same range. a) at $\gamma = 5$, for which the axial ratio of the strain ellipse in the matrix is $R_s = 27.0$ (indicated by the horizontal green line), with the long axis of this strain ellipse making an angle $\theta' = 10.9°$ with the shear direction (vertical green line); b) at $\gamma = 10$, for which $R_s = 102$ (off the vertical scale), with $\theta' = 5.7°$ (vertical green line); c) at $\gamma = 20$, for which $R_s = 402$ (off the vertical scale), with $\theta' = 2.9°$ (vertical green line); d) at $\gamma = 100$, for which $R_s \sim 10^4$ (off the vertical scale), with $\theta' = 0.57°$ (vertical green line). Note that even for this enormous R_s, many inclusions have maintained a rather low axial ratio, with $R_f < 3$, and the complete range in possible orientations, i.e. $-90° \leq \psi_f \leq 90°$. Elongate particles ($R_f > \sim 20$) are tightly oriented very close to the long axis of the matrix strain ellipse (and the shear plane) and would help define the mylonitic foliation. (For interpretation of the references to colour in this figure legend, the reader is referred to the web version of this article.)

of the matrix strain ellipse (and the shear plane) and would help define the mylonitic foliation of such a high strain shear zone; and (3) for moderate to high shear strains (Fig. 13a–c), particles with an intermediate axial ratio ($3\sim < R_f < \sim 20$) have a quasi-stable orientation with their long axes at a small synthetic angle to the foliation (i.e., a small negative angle in Fig. 13). Measurements on natural particle populations also show a transition from an effectively random orientation below $R_f < \sim 3$ to a strongly preferred orientation for larger R_f (Passchier, 1987; Pennacchioni et al., 2001; Mancktelow et al., 2002; Johnson et al., 2009). However, the (quasi-) stable orientation for intermediate R_f is at a small angle *antithetic* to the sense of shear (Pennacchioni et al., 2001; Mancktelow et al., 2002; ten Grotenhuis et al., 2002; Johnson et al., 2009), which is the opposite of what is predicted from Fig. 13. This difference may be explained by one or a combination of the following effects not considered in Fig. 13: (1) lack of coherence at the interface between inclusion and matrix (Ildefonse and Mancktelow, 1993; Pennacchioni et al., 2001; Mancktelow et al., 2002; Marques and Bose, 2004; Schmid and Podladchikov, 2004, 2005; Marques et al., 2005a; Mulchrone, 2007; Johnson et al., 2009); (2) limited width shear zone boundaries relative to the size of the inclusion (Marques and Coelho, 2001; Marques, 2005; Marques et al., 2005b); (3) strain localization in the matrix (ten Grotenhuis et al., 2002; Fay et al., 2008); and (4) interaction between adjacent particles (Ildefonse et al., 1992a, b; Jessell et al., 2009).

7. Conclusions

Compared to passive or rigid inclusions, deformable inclusions show a much greater variety in their behaviour. Power-law viscous rheology adds to this complexity, because the effective viscosity now varies with the inclusion orientation and axial ratio. Despite this added complexity, the overall behaviour is not fundamentally different. For a power-law inclusion, the overall form of the trajectories in an R-ψ plot, and therefore the R_f/ϕ plot that can be derived from it, is similar but not identical to that of a linear viscous system with a higher viscosity ratio than the viscosity ratio at the reference state. Comparable R-ψ plots can be generated by attempting to map stationary point(s). For a power-law viscous inclusion in a linear viscous matrix, the effective viscosity δ_{eff} at the stationary point is directly analogous to the linear viscous case. However, examples such as Fig. 6 with two stationary points and two different corresponding values of δ_{eff} emphasize the fact that such plots may be similar but cannot be identical. This difference reflects the variation in δ_{eff} with orientation and axial ratio R in the power-law case, which, for the specific orientation ψ_1 (dextral shear, or ψ_2 for sinistral shear) of stationary points, becomes more apparent as R increases (Fig. 5a), at least for low to moderate R values. As established above, as R becomes very large, the value of δ_{eff} tends asymptotically toward $(\delta_0)^{n_i}$ for inclusions with orientation $\psi_{1,2}$.

Introducing power-law viscous behaviour to the matrix again does not dramatically change the plots but further increases the contrast in effective viscosity between inclusion and matrix. For a stronger inclusion, the strain rate in the inclusion is lower, which increases the effective viscosity, and the strain rate in the adjacent matrix must on average be correspondingly higher, which decreases the effective viscosity, so that the effective viscosity ratio is increased. The opposite is obviously the case for a weaker inclusion. R-ψ plots can still be compared by mapping stationary points, determining the viscosity ratio that would produce a stationary point with the same axial ratio in the linear viscous case. Such plots remain similar in their fundamental characteristics, but differ in detail from those for a power-law viscous inclusion in a linear viscous matrix or for linear viscous behaviour of both inclusion and matrix. For a non-linear viscous matrix, stress and strain within the inclusion are no longer strictly homogeneous and the shape therefore does not remain perfectly elliptical. However, the differences are small except for very large elongations, when the shape becomes progressively more sigmoidal. For most applications, considering only low to moderate R_f, this minor heterogeneity induced by power-law viscosity in the matrix can be neglected.

For deformable but not purely passive inclusions, the final axial ratio R_f cannot be directly related to the strain in the matrix R_s. This is particularly true for more rotational flows ($W_k \rightarrow 1$) and the difference is increasingly marked for power-law viscous materials, due to the positive feedback between strain rate and effective viscosity ratio. The axial ratio R_f is also not directly related to the internal strain in the inclusion. This is of course true even for passive inclusions, as implicit in the standard R_f/ϕ technique. Many of the R-ψ trajectories for weakly elongate particles in rotational flows are oscillating, and nearly circular inclusions preserved in a natural shear zone can have had a long progressive strain history of extending and shortening that may be reflected in the internal microstructure, but not in the shape. Even for stationary orientations, where the orientation and axial ratio do not change, the internal strain rate is not zero and such inclusions can accumulate large internal finite strains while maintaining a low axial ratio and stable orientation.

The common observation in nature of rather equant "porphyroclasts" in highly deformed rocks, especially in shear zones, does not require nearly rigid behaviour. Even for low viscosity ratios at the reference state (e.g. $\delta_0 = 2–3$) and typical power-law stress exponents on the order of 3–6, as determined in experimental rock deformation experiments, originally weakly elongate inclusions ($R_i < 2$) can readily maintain a weakly elongate shape ($R_f < 3$ and, in many cases, $R_f < 2$) in high strain natural shear zones.

Acknowledgements

Reviews from D. Schmid and S. Johnson are gratefully acknowledged.

Appendix. Supplementary data

Supplementary data associated with this article can be found in online version at doi:10.1016/j.jsg.2011.06.005.

References

Arbaret, L., Diot, H., Bouchez, J.-L., 1996. Shape fabrics of particles in low concentration suspensions: 2D analogue experiments and application to tiling in magma. Journal of Structural Geology 18, 941–950.

Arbaret, L., Mancktelow, N.S., Burg, J.P., 2001. Effect of shape and orientation on rigid particle rotation and matrix deformation in simple shear flow. Journal of Structural Geology 23, 113–125.

Bilby, B.A., Eshelby, J.D., Kundu, A.K., 1975. The change of shape of a viscous ellipsoidal region embedded in a slowly deforming matrix having a different viscosity. Tectonophysics 28, 265–274.

Bilby, B.A., Kolbuszewski, M.L., 1977. The finite deformation of an inhomogeneity in two-dimensional slow viscous incompressible flow. Proceedings of the Royal Society of London, Series A 355, 335–353.

Bjørnerud, M.G., Zhang, H., 1995. Flow mixing, object-matrix coherence, mantle growth and the development of porphyroclast tails. Journal of Structural Geology 17, 1347–1350.

Bobyarchick, A.R., 1986. The eigenvalues of steady flow in Mohr space. Tectonophysics 122, 35–51.

Bretherton, F.P., 1962. The motion of rigid particles in shear flow at low Reynolds number. Journal of Fluid Mechanics 14, 284–301.

Ceriani, S., Mancktelow, N.S., Pennacchioni, G., 2003. Analogue modelling of the influence of shape and particle/matrix interface lubrication on the rotational behaviour of rigid particles in simple shear. Journal of Structural Geology 25, 2005–2021.

Deubelbeiss, Y., Kaus, B.J.P., Connolly, J.A.D., 2010. Direct numerical simulation of two-phase flow: effective rheology and flow patterns of particle suspensions. Earth and Planetary Science Letters 290, 1–12.
Dunnet, D., 1969. A technique of finite strain analysis using elliptical particles. Tectonophysics 7, 117–136.
Einstein, A., 1906. Eine neue Bestimmung der Moleküldimensionen. Annalen der Physik 19, 289–306.
Einstein, A., 1911. Berichtigung zu meiner Arbeit: "Eine neue Bestimmung der Moleküldimensionen". Annalen der Physik 34, 591–592.
Eshelby, J.D., 1957. The determination of the elastic field of an ellipsoidal inclusion and related problems. Proceedings of the Royal Society of London, Series A 241, 376–396.
Eshelby, J.D., 1959. The elastic field outside an ellipsoidal inclusion. Proceedings of the Royal Society of London, Series A 252, 561–569.
Fay, C., Bell, T.H., Hobbs, B.E., 2008. Porphyroblast rotation versus nonrotation: conflict resolution! Geology 36, 307–310.
Ferguson, C.C., 1979. Rotations of elongate rigid particles in slow non-Newtonian flows. Tectonophysics 60, 247–262.
Fernandez, A., Feybesse, J.L., Mezure, J.F., 1983. Theoretical and experimental study of fabric developed by different shaped markers in two-dimensional simple shear. Bulletin de la Société Géologique de France 25, 319–326.
Fletcher, R.C., 2004. Anisotropic viscosity of a dispersion of aligned elliptical cylindrical clasts in viscous matrix. Journal of Structural Geology 26, 1977–1987.
Fletcher, R.C., 2009. Deformable, rigid, and inviscid elliptical inclusions in a homogeneous incompressible anisotropic viscous fluid. Journal of Structural Geology 31, 382–387.
Freeman, B., 1985. The motion of rigid ellipsoidal particles in slow flows. Tectonophysics 113, 163–183.
Gay, N.C., 1968. The motion of rigid particles embedded in a viscous fluid during pure shear deformation of the fluid. Tectonophysics 5, 81–88.
Ghosh, S.K., Ramberg, H., 1976. Reorientation of inclusions by combination of pure shear and simple shear. Tectonophysics 34, 1–70.
Ghosh, S.K., Sengupta, S., 1973. Compression and simple shear of test models with rigid and deformable inclusions. Tectonophysics 17, 133–175.
Gierszewski, P.J., Chaffey, C.E., 1978. Rotation of an isolated triaxial ellipsoid suspended in slow viscous flow. Canadian Journal of Physics 56, 6–11.
Gilormini, P., Germain, Y., 1987. A finite element analysis of the inclusion problem for power law viscous materials. International Journal of Solids and Structures 23, 413–437.
Gilormini, P., Montheillet, F., 1986. Deformation of an inclusion in a viscous matrix and induced stress concentrations. Journal of the Mechanics and Physics of Solids 34, 97–123.
Goddard, J.D., Miller, C., 1967. Nonlinear effects in the rheology of dilute suspensions. Journal of Fluid Mechanics 28, 657–673.
Grujic, D., Mancktelow, N.S., 1998. Melt-bearing shear zones: analogue experiments and comparison with examples from southern Madagascar. Journal of Structural Geology 20, 673–680.
Hanna, S.S., Fry, N., 1979. A comparison of methods of strain determination in rocks from southwest Dyfed (Pembrokeshire) and adjacent areas. Journal of Structural Geology 1, 155–162.
Hinch, E.J., Leal, L.G., 1979. Rotation of small non-axisymmetric particles in a simple shear flow. Journal of Fluid Mechanics 92, 591–608.
Howard, I.C., Brierley, P., 1976. On the finite deformation of an inhomogeneity in a viscous liquid. International Journal of Engineering Science 14, 1151–1159.
Ildefonse, B., Fernandez, A., 1988. Influence of the concentration of rigid markers in a viscous medium on the production of preferred orientations. An experimental contribution, 1. Non coaxial strain. In: Talbot, C.J. (Ed.), Geological Kinematics and Dynamics (In Honor of the 70th Birthday of Hans Ramberg). Bulletin of the Geological Institutions of the University of Uppsala, vol. 14, pp. 55–60.
Ildefonse, B., Launeau, P., Fernandez, A., Bouchez, J.L., 1992a. Effect of mechanical interactions on development of shape preferred orientations: a two-dimensional experimental approach. Journal of Structural Geology 14, 73–83.
Ildefonse, B., Mancktelow, N.S., 1993. Deformation around rigid particles: the influence of slip at the particle/matrix interface. Tectonophysics 221, 345–359.
Ildefonse, B., Sokoutis, D., Mancktelow, N.S., 1992b. Mechanical interactions between rigid particles in a deforming ductile matrix. Analogue experiments in simple shear flow. Journal of Structural Geology 14, 1253–1266.
Jeffery, G.B., 1922. The motion of ellipsoidal particles immersed in a viscous fluid. Proceedings of the Royal Society of London, Series A 102, 161–179.
Jessell, M.W., Bons, P.D., Griera, A., Evans, L.A., Wilson, C.J.L., 2009. A tale of two viscosities. Journal of Structural Geology 31, 719–736.
Ježek, J., 1994. Software for modeling the motion of rigid triaxial ellipsoidal particles in viscous-flow. Computers & Geosciences 20, 409–424.
Ježek, J., Melka, R., Schulmann, K., Venera, Z., 1994. The behaviour of rigid triaxial ellipsoidal particles in viscous flows – modeling of fabric evolution in a multiparticle system. Tectonophysics 229, 165–180.
Ježek, J., Schulmann, K., Segeth, K., 1996. Fabric evolution of rigid inclusions during mixed coaxial and simple shear flows. Tectonophysics 257, 203–221.
Jiang, D., 2007a. Numerical modeling of the motion of rigid ellipsoidal objects in slow viscous flows: a new approach. Journal of Structural Geology 29, 189–200.
Jiang, D., 2007b. Numerical modeling of the motion of deformable ellipsoidal objects in slow viscous flows. Journal of Structural Geology 29, 435–452.
Jiang, D., 2010. Flow and finite deformation of surface elements in three dimensional homogeneous progressive deformations. Tectonophysics 487, 85–99.
Jiang, D., in press. A general approach for modeling the motion of rigid and deformable ellipsoids in ductile flows. Computers & Geosciences. doi:10.1016/j.cageo.2011.05.002.
Johnson, S.E., Lenferink, H.J., Price, N.A., Marsh, J.H., Koons, P.O., West Jr., D.P., Beane, R., 2009. Clast-based kinematic vorticity gauges: the effects of slip at matrix/clast interfaces. Journal of Structural Geology 31, 1322–1339.
Kohlstedt, D.L., Evans, B., Mackwell, S.J., 1995. Strength of the lithosphere: constraints imposed by laboratory experiments. Journal of Geophysical Research 100, 17587–17602.
Lisle, R.J., 1985. Geological Strain Analysis. A Manual for the R_f /Ø Technique. Pergamon Press, Oxford, United Kingdom.
Lister, G.S., Williams, P.F., 1983. The partitioning of deformation in flowing rock masses. Tectonophysics 92, 1–33.
Mancktelow, N.S., 1993. Tectonic overpressure in competent mafic layers and the development of isolated eclogites. Journal of Metamorphic Geology 11, 801–812.
Mancktelow, N.S., 2002. Finite-element modelling of shear zone development in viscoelastic materials and its implications for localisation of partial melting. Journal of Structural Geology 24, 1045–1053.
Mancktelow, N.S., 2006. How ductile are ductile shear zones? Geology 34, 345–348.
Mancktelow, N.S., 2008. Tectonic pressure: theoretical concepts and modelled examples. Lithos 103, 149–177.
Mancktelow, N.S., Arbaret, L., Pennacchioni, G., 2002. Experimental observations on the effect of interface slip on rotation and stabilisation of rigid particles in simple shear and a comparison with natural mylonites. Journal of Structural Geology 24, 567–585.
Mancktelow, N.S., Pennacchioni, G., 2010a. Why calcite can be stronger than quartz. Journal of Geophysical Research 115, B01402.
Mancktelow, N.S., Pennacchioni, G., 2010b. Correction to "Why calcite can be stronger than quartz". Journal of Geophysical Research 115, B10410.
Mandal, N., Misra, S., Samanta, S.K., 2005a. Rotation of single rigid inclusions embedded in an anisotropic matrix: a theoretical study. Journal of Structural Geology 27, 731–743.
Mandal, N., Samanta, S.K., Bhattacharyya, G., Chakraborty, C., 2003. Deformation of ductile inclusions in a multiple inclusion system in pure shear. Journal of Structural Geology 25, 1359–1370.
Mandal, N., Samanta, S.K., Bhattacharyya, G., Chakraborty, C., 2005b. Rotation behaviour of rigid inclusions in multiple association: insights from experimental and theoretical models. Journal of Structural Geology 27, 679.
Mandal, N., Samanta, S.K., Chakraborty, C., 2005c. Numerical models of flow patterns around a rigid inclusion in a viscous matrix undergoing simple shear: implications of model parameters and boundary conditions. Journal of Structural Geology 27, 1599–1609.
Marques, F.O., 2005. Effects of confinement on matrix flow around a rigid inclusion in viscous simple shear: insights from analogue and numerical modelling. Journal of Structural Geology 27, 379–396.
Marques, F.O., Bose, S., 2004. Influence of a permanent low-friction boundary on rotation and flow in rigid inclusion/viscous matrix systems from an analogue perspective. Tectonophysics 382, 229–245.
Marques, F.O., Cobbold, P.R., 1995. Development of highly non-cylindrical folds around rigid ellipsoidal inclusions in bulk simple shear regimes: natural examples and experimental modeling. Journal of Structural Geology 17, 589–602.
Marques, F.O., Coelho, S., 2001. Rotation of rigid elliptical cylinders in viscous simple shear flow: analogue experiments. Journal of Structural Geology 23, 609–617.
Marques, F.O., Taborda, R., Antunes, J., 2005a. Influence of a low-viscosity layer between rigid inclusion and viscous matrix on inclusion rotation and matrix flow: a numerical study. Tectonophysics 407, 101–115.
Marques, F.O., Taborda, R., Bose, S., Antunes, J., 2005b. Effects of confinement on matrix flow around a rigid inclusion in viscous simple shear: insights from analogue and numerical modelling. Journal of Structural Geology 27, 379–396.
Marques, F.O., Taborda, R.M., Antunes, J.V., 2005c. 2D rotation of rigid inclusions in confined bulk simple shear flow: a numerical study. Journal of Structural Geology 27, 2171–2180.
Means, W.D., Hobbs, B.E., Lister, G.S., Williams, P.F., 1980. Vorticity and non-coaxiality in progressive deformation. Journal of Structural Geology 2, 371–378.
Mulchrone, K.F., 2007. An analytical solution in 2D for the motion of rigid elliptical particles with a slipping interface under a general deformation. Journal of Structural Geology 29, 950–960.
Mulchrone, K.F., Walsh, K., 2006. The motion of a non-rigid ellipse in a general 2D deformation. Journal of Structural Geology 28, 392–407.
Muskhelishvili, N.I., 1953. Some Basic Problems of the Mathematical Theory of Elasticity. Noordhoff, Groningen.
Passchier, C.W., 1987. Stable positions of rigid objects in non-coaxial flow – a study in vorticity analysis. Journal of Structural Geology 9, 679–690.
Passchier, C.W., Mancktelow, N.S., Grasemann, B., 2005. Flow perturbations: a tool to study and characterize heterogeneous deformation. Journal of Structural Geology 27, 1011–1026.
Passchier, C.W., Simpson, C., 1986. Porphyroclast systems as kinematic indicators. Journal of Structural Geology 8, 831–843.
Passchier, C.W., Sokoutis, D., 1993. Experimental modelling of mantle porphyroclasts. Journal of Structural Geology 15, 895–909.

Passchier, C.W., ten Brink, C.E., Bons, P.D., Sokoutis, D., 1993. δ objects as a gauge for stress sensitivity of strain rate in mylonites. Earth and Planetary Science Letters 120, 239–245.
Passchier, C.W., Trouw, R.A.J., 2005. Microtectonics. Springer, Berlin.
Pennacchioni, G., Di Toro, G., Mancktelow, N.S., 2001. Strain-insensitive preferred orientation of porphyroclasts in Mont Mary mylonites. Journal of Structural Geology 23, 1281–1298.
Pennacchioni, G., Fasolo, L., Cecchi, M.M., Salasnich, L., 2000. Finite-element modelling of simple shear flow in Newtonian and non-Newtonian fluids around a circular rigid particle. Journal of Structural Geology 22, 683–692.
Piazolo, S., Bons, P.D., Passchier, C.W., 2002. The influence of matrix rheology and vorticity on fabric development of populations of rigid objects during plane strain deformation. Tectonophysics 351, 315–329.
Piazolo, S., Passchier, C.W., 2002. Experimental modeling of viscous inclusions in a circular high-strain shear rig: implications for the interpretation of shape fabrics and deformed enclaves. Journal of Geophysical Research 107, 2242.
Ramberg, H., 1975a. Particle paths, displacement and progressive strain applicable to rocks. Tectonophysics 28, 1173–1187.
Ramberg, H., 1975b. Superposition of homogeneous strain and progressive deformation in rocks. Bulletin of the Geological Institutions of the University of Uppsala 6, 35–67.
Ramsay, J.G., 1967. Folding and Fracturing of Rocks. McGraw-Hill, New York.
Ramsay, J.G., Huber, M.I., 1983. The Techniques of Modern Structural Geology. Volume 1: Strain Analysis. Academic Press, London.
Ranalli, G., 1995. Rheology of the Earth, second ed. Chapman & Hall, London.
Robinson, K., 1951. Elastic energy of an ellipsoidal inclusion in an infinite solution. Journal of Applied Physics 22, 1045–1054.
Roscoe, R., 1967. On the rheology of a suspension of viscoelastic spheres in a viscous fluid. Journal of Fluid Mechanics 28, 273–293.
Schmalholz, S.M., Schmid, D.W., Fletcher, R.C., 2008. Evolution of pinch-and-swell structures in a power-law layer. Journal of Structural Geology 30, 649–663.
Schmid, D.W., 2005. Rigid polygons in shear. In: Bruhn, D., Burlini, L. (Eds.), High-strain Zones. Structure and Physical Properties. Geological Society London Special Publications, vol. 245, pp. 421–431.
Schmid, D.W., Podladchikov, Y.Y., 2003. Analytical solutions for deformable elliptical inclusions in general shear. Geophysical Journal International 155, 269–288.
Schmid, D.W., Podladchikov, Y.Y., 2004. Are isolated stable rigid clasts in shear zones equivalent to voids? Tectonophysics 384, 233–242.
Schmid, D.W., Podladchikov, Y.Y., 2005. Mantled porphyroclast gauges. Journal of Structural Geology 27, 571–585.
Schmid, D.W., Podladchikov, Y.Y., Marques, F.O., 2004. Folding of a finite length power law layer. Journal of Geophysical Research 109, B03407.
Spence, D.A., Wilmott, P., 1988. Rotation and deformation of a viscous inclusion in Stokes-flow. Proceedings of the Royal Society of London, Series A 418, 383–403.
Strömgård, K.-E., 1973. Stress distribution during formation of boudinage and pressure shadows. Tectonophysics 16, 215–248.
ten Brink, C.E., Passchier, C.W., 1995. Modelling of mantled porphyroclasts using non-Newtonian rock analogue materials. Journal of Structural Geology 17, 131–146.
ten Grotenhuis, S.M., Passchier, C.W., Bons, P.D., 2002. The influence of strain localisation on the rotation behaviour of rigid objects in experimental shear zones. Journal of Structural Geology 24, 485–499.
Treagus, S.H., 1973. Buckling stability of a viscous single-layer system, oblique to the principal compression. Tectonophysics 19, 271–289.
Treagus, S.H., Lan, L., 2003. Simple shear of deformable square objects. Journal of Structural Geology 25, 1993–2003.
Treagus, S.H., Treagus, J.E., 2002. Studies of strain and rheology of conglomerates. Journal of Structural Geology 24, 1541–1567.
Truesdell, C., 1953. Two measures of vorticity. Journal of Rational Mechanics and Analysis 2, 173–217.
Willis, D.G., 1977. A kinematic model of preferred orientation. Geological Society of America Bulletin 88, 883–894.